Geometrically nonlinear polygonal finite element analysis of functionally graded porous plates

Nam V. Nguyen[1], Hoang X. Nguyen[2], Seunghye Lee[3], H. Nguyen-Xuan[4,5*]

[1]*Faculty of Mechanical Technology, Industrial University of Ho Chi Minh City, Vietnam*

[2]*Department of Mechanical and Construction Engineering, Northumbria University, Newcastle upon Tyne NE1 8ST, United Kingdom*

[3]*Department of Architectural Engineering, Sejong University, 209 Neungdong-ro, Gwangjin-gu, Seoul 05006, Republic of Korea*

[4]*CIRTech Institute, Ho Chi Minh City University of Technology (HUTECH), Ho Chi Minh City, Vietnam*

[5]*Department of Physical Therapy, Graduate Institute of Rehabilitation Science, China Medical University, Taichung 40402, Taiwan*

Abstract

In this study, an efficient polygonal finite element method (PFEM) in combination with quadratic serendipity shape functions is proposed to study nonlinear static and dynamic responses of functionally graded (FG) plates with porosities. Two different porosity types including even and uneven distributions through the plate thickness are considered. The quadratic serendipity shape functions over arbitrary polygonal elements including triangular and quadrilateral ones, which are constructed based on a pairwise product of linear shape functions, are employed to interpolate the bending strains. Meanwhile, the shear strains are defined according to the Wachspress coordinates. By using the Timoshenko's beam to interpolate the assumption of the strain field along the edges of polygonal element, the shear locking phenomenon can be naturally eliminated. Furthermore, the C^0–type higher-order shear deformation theory (C^0–HSDT), in which two additional variables are included in the displacement field, significantly improves the accuracy of numerical results. The nonlinear equations of static and dynamic problems are solved by Newton-Raphson iterative procedure and by Newmark's integration scheme in association with the Picard methods, respectively. Through various numerical examples in which complex geometries and different boundary conditions are involved, the proposed approach yields more stable and accurate results than those generated using other existing approaches.

Keywords: Polygonal finite element method, Quadratic serendipity shape functions, Functionally graded materials, Porosity, Timoshenko's beam, Nonlinear dynamics.

[*]Corresponding author, Tel: +84 906682393. *Email address*: ngx.hung@hutech.edu.vn (H. Nguyen-Xuan).

1. Introduction

Functionally graded materials (FGMs) are categorized as a special class of composite materials [1] because they are formed of two or more constituent phases of distinct materials. As the material properties change continuously and smoothly from one surface to another, FGMs are capable of eliminating stress concentration and delamination phenomena which generally encountered in conventional laminated composites. Based on advantageous properties of ceramic and metal such as resistant to high temperatures and ductility, respectively, FGMs are commonly synthesized from these material phases. Thanks to these striking features, FGMs have been extensively applied to various engineering applications including aerospace, defence, automotive, nuclear power, bio-engineering and other areas [2, 3]. There have been extensive efforts working on the analysis of FG structures in the literature [4-10]. Due to technical issues during the manufacturing process, porosities may appear within the FGMs and cause reduction in the strength of the materials. Wattanasakulpong et al. [11] reported that there are porosities existing in the middle area of the FGM samples which are fabricated by using multi-step sequential infiltration technique. Therefore, it is indispensable to consider porosity effects when investigating the nonlinear static and dynamic responses of FGM structures. In the literature, there are many studies that take into consideration the FGM structures with porosities. However, most of these investigations focus on the vibration behavior of porous FG structures such as beams [12, 13], plate structures [14-16] and shell structures [17]. Additionally, the buckling problems of porous FG beams and plates have also been discussed [18, 19]. Based on the quasi-3D shear deformation theory, Zenkour [20] investigated the bending responses of porous FG single-layered and sandwich plates which are graded using two types of exponential or polynomial laws.

Due to the limitations of the three–dimensional (3D) model when solving practical problems with complex geometries under arbitrary boundary conditions, several two–dimensional (2D) model plate theories have been developed and widely employed to predict appropriately the structural responses. The classical plate theory (CPT), which was devised based on the Kirchhoff–Love assumptions, is the most fundamental plate theory. Even though this theory works well for thin plates in which the length-to-thickness ratio is large, it may lead to inaccurate predictions as it ignores the shear deformations. First-order shear deformation theory (FSDT) [21, 22] which considers the transverse shear deformation effects, has been suitably developed for both thin and thick plates. However, this theory requires an appropriate shear correction factor whose value depends on various factors such as applied

loads, boundary conditions, material coefficients and geometric, to satisfy the traction-free boundary conditions at surfaces of the plate. In order to surmount the limitations in CPT and FSDT, a large number of different higher-order shear deformation theories (HSDTs) have been developed such as third-order shear deformation theory (TSDT) [23, 24], sinusoidal shear deformation theory [25], hyperbolic shear deformation theory (HSDT) [26, 27], refined plate theories (RPT) [28], and some higher-order theories based on Carrera's Unified Formulation (CUF) [29, 30]. However, the HSDTs require C^1–continuity of the generalized displacements that cause challenges in calculation of second-order derivatives of deflections if one uses conventional finite element analysis. In an effort to overcome this obstacle, Shankara and Iyengar [31] proposed the C^0–type higher-order shear deformation theory (C^0–HSDT) in which two variables are added to the displacements and only the first derivatives of deflection are required.

In 2D finite element analysis, the most frequently used element types are triangles and quadrilaterals. Nevertheless, it was pointed out that when treating complex microstructures modeling or material design, significant troubles in generating quality meshes may remain. For example, in polycrystalline materials, each crystal is usually considered as the polygon. By using the conventional triangular and quadrilateral elements to discretize these microstructures, the high resolution of meshes is required. Fortunately, the drawbacks can be easily treated in PFEM by modeling each crystal as one polygonal element. Therefore, many researchers have been focusing on developing the generalizations of FEM which rely on arbitrary polygonal meshes and include both triangular and quadrilateral elements. In terms of computation, PFEM is more flexible in discretization, useful in mesh transitions and refinement, well-suited for material design and sometimes more accurate and robust in approximating results [32]. In recent years, PFEM has been widely applied in many mechanical problems such as nonlinear behavior of polycrystalline materials [33-35], nonlinear elastic materials [32, 36], incompressible fluid flow [37, 38], crack modeling [39, 40], limit analysis [41], topology optimization [42-44], contact-impact problem [45. In terms of plate analysis, Nguyen-Xuan [46] firstly proposed a Reissner–Mindlin plate formula that is suitable for both thick and thin plates on arbitrary polygonal meshes based on the Timoshenko's beam assumptions. In this work, four barycentric shape function types such as Wachspress, mean–value, Laplace and piecewise–linear are considered. Then, using the piecewise–linear shape function, Nguyen *et al.* [47] extended a polygonal finite element to laminated composite plates based on the C^0 approximations (C^0–HSDT). Our current study

aims to improve the performance of the original polygonal plate element [46] and we then apply it to nonlinear analysis of porous FG plates.

Compared with the traditional finite elements, the construction of shape functions over arbitrary polygon elements is not easy due to the complexity of the general polygonal element shape. Therefore, numerous approaches have been proposed to determine the shape functions for polygonal elements such as the rational polynomial interpolation functions proposed by Wachspress firstly [48], mean value coordinates by Floater [49], maximum entropy coordinates by Sukumar [50], natural neighbor interpolants by Sukumar et al. [51], moving least squares coordinates [52], the sharp upper and lower bound piecewise-linear functions by Floater et al. [53], etc. The outline the construction of polygonal shape functions is presented by Sukumar and Malsch [54]. Recently, the development to higher-order approximations over arbitrary polygonal elements has been attracting high level of attention. Using pairwise product of linear shape functions, Rand et al. [55] proposed the construction process of the quadratic serendipity shape functions over convex polygonal element based on generalized barycentric coordinates. Herein, the nodal shape functions are only associated with the vertices and the mid-nodes on the edges of polygonal element. Sellam et al. [56] employed the quadratic serendipity polygonal elements for generalized elastic solids subjected to torsion. Heng et al. [57] utilized a general gradient correction scheme for serendipity element in finite elasticity problems. Based on the local generalized barycentric coordinates and triangular coordinates, Floater and Lai [58] presented polygonal splines which Sinu et al. [59] further developed for constructing serendipity shape functions over hexahedra and convex polyhedral. In addition, Sukumar [60] proposed the quadratic maximum-entropy serendipity shape functions for both convex and nonconvex polygons.

In an effort to improve the numerical results and construct a unified formula for the arbitrary polygonal finite element including triangular and quadrilateral elements, in this study, we propose an effective and novel unified formulation for both thick and thin plate elements on arbitrary polygonal meshes. In order to get results that are more accurate, the quadratic serendipity shape functions are enhanced to the arbitrary polygonal finite element formulation. In addition, based on Soh's works [61,62] which only were available for triangular and quadrilateral elements, the Timoshenko's beam theory is applied to interpolate the assumption of strain field along sides of arbitrary polygonal element. As a result, the shear locking phenomenon can be naturally suppressed. According to polygonal elements, the bending strains are computed using the quadratic serendipity shape functions while the shear strains

employ the Wachspress coordinates at the vertices on polygonal elements. The static and dynamic analyses of porous FG plates including both linear and geometrically nonlinear cases are performed to demonstrate the superiority in terms of the efficiency and accuracy of the present method. Two types of porosity distribution including even and uneven distributions with various porosity volume fractions are considered in numerical examples. The impact of a few specific parameters such as different porosity distribution, porosity volume fraction, material index and thickness ratio on the deflection of porous FG plates, is considered and discussed in detail. As shown in the numerical examples, the proposed element, which based on the quadratic serendipity shape functions, shows more accurate and stable than those of other PFEMs, which were reported in [46]. It should be noted that the mid-side nodes of the quadratic serendipity polygonal element are then eliminated in the calculation process, which leads to the number of DOFs per polygonal element does not increase when compared with the formulation given in [46].

The remaining of this study is organized as follows. A brief review of the FGM with porosities, the C^0-HSDT type as well as a weak form of governing equations of porous FG plate for static and dynamic problems is presented in the next section. The formulations of the PFEM for porous FG plates with the quadratic serendipity shape functions based on the Timoshenko's beam formulation are given in Section 3. The numerical examples for static and dynamic analysis, which include both linear and geometrically nonlinear cases, of porous FG plates are presented in Section 4. Finally, Section 5 closes this study with some concluding remarks.

2. C^0-type higher-order shear deformation plate theory for porous FG plates

2.1 Functionally graded materials with porosities

The model of an FG plate which consists of metal and ceramic is depicted in Fig. 1a. This FG plate contains porosities in its structure, which can be dispersed evenly or unevenly along the plate thickness direction, as shown in Fig. 1b. Based on the rule of mixtures [63], the modified effective material properties throughout the thickness of the FG plates, which assumed porosities disperse evenly in the metal and ceramic phases can be given as [12]

$$P\left(z\right) = P_m\left(V_m - \frac{\alpha}{2}\right) + P_c\left(V_c - \frac{\alpha}{2}\right), \tag{1}$$

where α $(0 \le \alpha \ll 1)$ is a porosity volume fraction, this parameter is set to zero for FG plate without porosities which is usually called the perfect FG plates. Meanwhile P_m and P_c represent the typical material properties of the metal and ceramic phases, respectively, including the Young's modulus E, the Poisson's ratio ν and the density ρ. The volume fractions of metal V_m and ceramic V_c phases, respectively, are assumed to vary with respect to the thickness h, which are defined as follows

$$V_c(z) = \left(\frac{1}{2} + \frac{z}{h}\right)^n, \quad \mathrm{V}_m = 1 - V_c, \quad \frac{-h}{2} \le z \le \frac{h}{2}, \tag{2}$$

in which n is the material index describing the profile of material variation. It is worth noting that setting n to 0 leads to a single-phase ceramic material while a homogeneous metallic material is obtained as n increases towards $+\infty$.

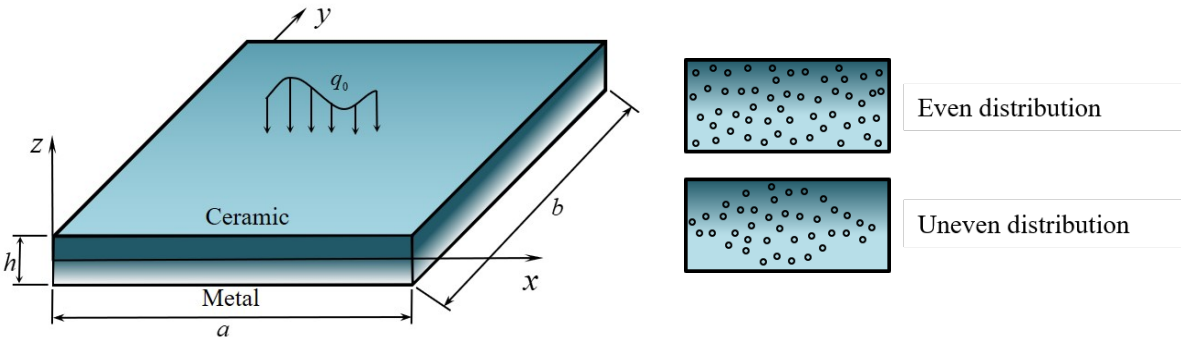

(a) (b)

Fig. 1. (a) The FG plate model made of ceramic and metal with porosities
(b) Plate cross-section for two porosity distributions.

Then, the modified effective material properties for the ceramic-metal FG plates with evenly distributed porosities are given by

$$P(z) = (P_c - P_m)\left(\frac{1}{2} + \frac{z}{h}\right)^n + P_m - \frac{\alpha}{2}(P_c + P_m). \tag{3}$$

Similarly, the modified effective material properties of ceramic-metal FG plates with unevenly distributed porosities can be expressed as [12]

$$P(z) = (P_c - P_m)\left(\frac{1}{2} + \frac{z}{h}\right)^n + P_m - \frac{\alpha}{2}(P_c + P_m)\left(1 - \frac{2|z|}{h}\right). \tag{4}$$

Fig. 2 illustrates the variation in effective Young's modulus of the prefect and porous for ceramic-metal FG (Al/Al_2O_3) plates estimated based on the rule of mixtures with a porosity volume fraction $\alpha = 0.3$. It can be seen that Young's modulus of the perfect FG plate is highest while the porous FG plate with even distribution has the lowest magnitude. Furthermore, the effective Young's modulus of perfect FG and porous FG with uneven distribution plates coincides at the top and bottom surface of the plate while it coincides at the middle surface of two porous FG plates.

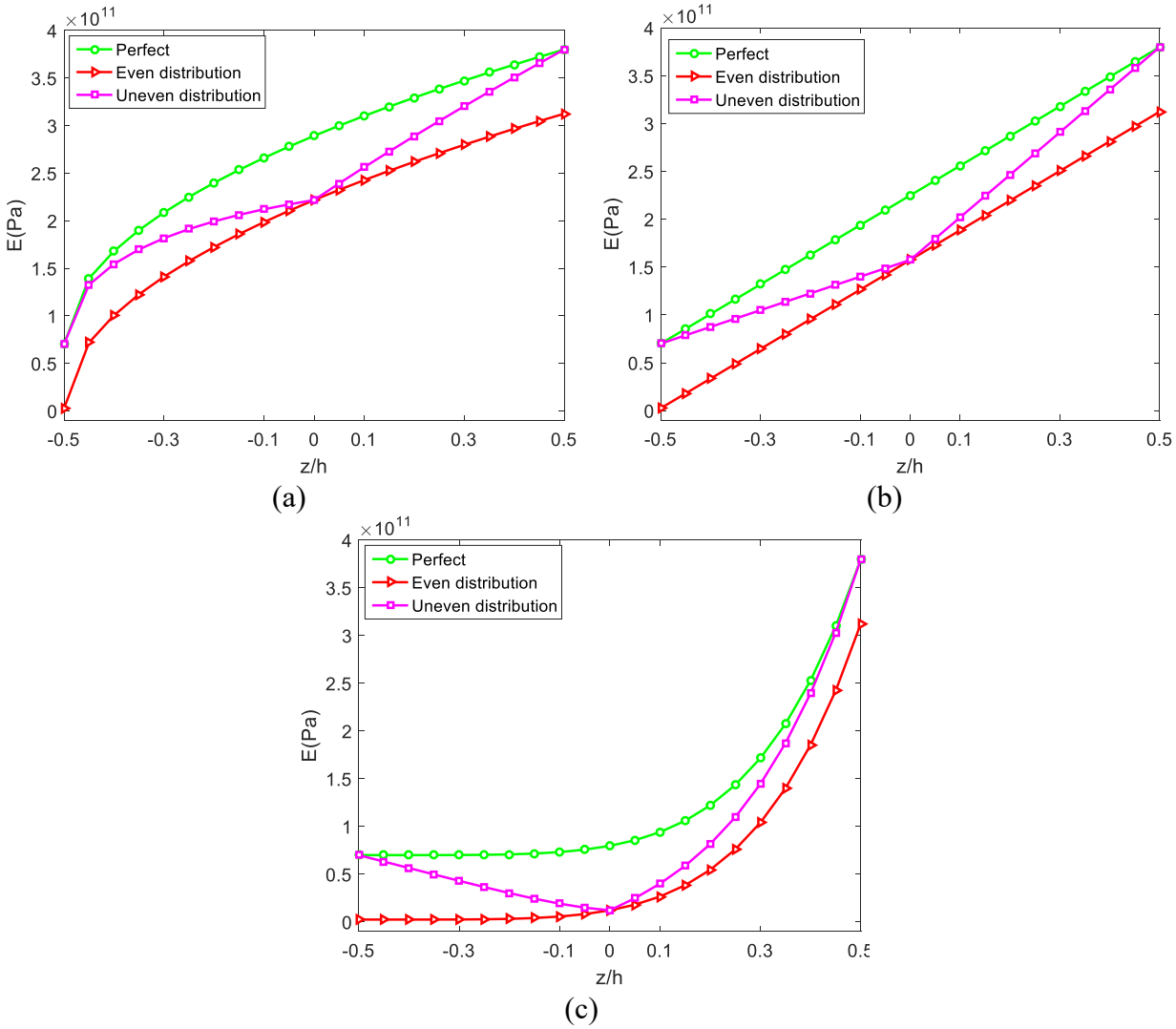

Fig. 2. Variations of Young's modulus of perfect and porous FG plates with $\alpha = 0.3$: (a) $n = 0.5$; (b) $n = 1$; (c) $n = 5$.

2.2 C^0-type higher-order shear deformation plate theory

Based on the C^0-HSDT model [31], the displacement fields at an arbitrary point in the plate can be defined as follows

$$
\begin{aligned}
u(x,y,z) &= u_0 + z\beta_x + cz^3\left(\beta_x + \phi_x\right),\\
v(x,y,z) &= v_0 + z\beta_y + cz^3\left(\beta_y + \phi_y\right), \quad \left(-\frac{h}{2} \le z \le \frac{h}{2}\right),\\
w(x,y,z) &= w_0,
\end{aligned} \tag{5}
$$

where u_0, v_0 and w_0 are the displacements of a point on the mid-plane of the plate, respectively; β_x and β_y denote the rotations of the normal to the mid-plane about the y and x axes, respectively; and $c = -4/3h^2$. Eq. (5) is developed from the higher-order theory by Reddy [23], in which derivative of deflection is replaced by warping function $\boldsymbol{\phi} = \left\{\phi_x, \phi_y\right\}^T$. The generalized displacement vector with 5 degrees of freedom for C^1-continuity element can be transformed to a vector with 7 degrees of freedom for C^0-continuity element $\mathbf{u} = \left\{u_0, v_0, w, \beta_x, \beta_y, \phi_x, \phi_y\right\}^T$.

For large deformation analysis, the in-plane vector of Green's strain can be written in compact form as follow:

$$
\varepsilon_{ij} = \frac{1}{2}\left(\frac{\partial u_i}{\partial x_j} + \frac{\partial u_j}{\partial x_i} + \frac{\partial u_k}{\partial x_i}\frac{\partial u_k}{\partial x_j}\right). \tag{6}
$$

By substituting Eq. (5) into Eq. (6) and adopting the von Kármán assumptions [64], the strain-displacement relations in Eq. (6) can be rewritten as

$$
\boldsymbol{\varepsilon} = \left\{\varepsilon_x, \varepsilon_y, \gamma_{xy}\right\}^T = \boldsymbol{\varepsilon}_0 + z\boldsymbol{\kappa}_1 + z^3\boldsymbol{\kappa}_2, \tag{7}
$$

where the membrane strain is given by

$$
\boldsymbol{\varepsilon}_0 = \boldsymbol{\varepsilon}_0^L + \boldsymbol{\varepsilon}_0^{NL}, \tag{8}
$$

in which $\boldsymbol{\varepsilon}_0^L$ and $\boldsymbol{\varepsilon}_0^{NL}$ are linear and nonlinear parts of the in-plane strains, respectively. Meanwhile $\boldsymbol{\kappa}_1$ and $\boldsymbol{\kappa}_2$ are bending strains. The shear strains can be expressed as:

$$
\boldsymbol{\gamma} = \left\{\gamma_{xz}, \gamma_{yz}\right\}^T = \boldsymbol{\varepsilon}_s + z^2\boldsymbol{\kappa}_s, \tag{9}
$$

After adopting the derivation of the Hamilton's principal and weak formulation, the weak form of the nonlinear problem of FG plates under transverse load q_0 can be briefly expressed as

$$
\int_\Omega \delta\hat{\boldsymbol{\varepsilon}}^T \mathbf{D}^* \hat{\boldsymbol{\varepsilon}}\, d\Omega + \int_\Omega \delta\hat{\boldsymbol{\gamma}}^T \mathbf{D}_s^* \hat{\boldsymbol{\gamma}} d\Omega = \int_\Omega \delta w q_0 d\Omega, \tag{10}
$$

in which $\hat{\boldsymbol{\varepsilon}}$ includes in-plane and bending strains and $\hat{\boldsymbol{\gamma}}$ represents shear strains.

The material constant matrices $\mathbf{D}^*$ and $\mathbf{D}_s^*$ can be defined as follows

$$\mathbf{D}^* = \begin{bmatrix} \mathbf{A} & \mathbf{B} & \mathbf{E} \\ \mathbf{B} & \mathbf{D} & \mathbf{F} \\ \mathbf{E} & \mathbf{F} & \mathbf{H} \end{bmatrix}, \quad \mathbf{D}_s^* = \begin{bmatrix} \mathbf{A}^s & \mathbf{B}^s \\ \mathbf{B}^s & \mathbf{D}^s \end{bmatrix}, \tag{11}$$

in which

$$\begin{aligned} &\left(A_{ij}, B_{ij}, D_{ij}, E_{ij}, F_{ij}, H_{ij}\right) = \int_{-h/2}^{h/2} \left(1, z, z^2, z^3, z^4, z^6\right) Q_{ij} dz, && \left(i, j = 1,2,6\right), \\ &\left(A_{ij}^s, B_{ij}^s, D_{ij}^s\right) = \int_{-h/2}^{h/2} \left(1, z^2, z^4\right) Q_{ij} dz, && \left(i, j = 4,5\right). \end{aligned} \tag{12}$$

For nonlinear transient analysis, the weak form of FG plate under transverse load q_0 without damping effect can be written as

$$\int_\Omega \delta \mathbf{u}^T \mathbf{m} \ddot{\mathbf{u}} d\Omega + \int_\Omega \delta \hat{\boldsymbol{\varepsilon}}^T \mathbf{D}^* \hat{\boldsymbol{\varepsilon}}_p d\Omega + \int_\Omega \delta \hat{\boldsymbol{\gamma}}^T \mathbf{D}_s^* \hat{\boldsymbol{\gamma}} d\Omega = \int_\Omega \delta w q_0 d\Omega. \tag{13}$$

where the mass matrix **m** is given as

$$\mathbf{m} = \begin{bmatrix} I_1 & 0 & 0 & I_2 & 0 & c/3I_4 & 0 \\ & I_1 & 0 & 0 & I_2 & 0 & c/3I_4 \\ & & I_1 & 0 & 0 & 0 & 0 \\ & & & I_3 & 0 & c/3I_5 & 0 \\ & & & & I_3 & 0 & c/3I_5 \\ & & & & & c^2/9I_7 & 0 \\ \text{sym.} & & & & & & c^2/9I_7 \end{bmatrix}, \tag{14}$$

in which $\left(I_1, I_2, I_3, I_4, I_5, I_7\right) = \int_{-h/2}^{h/2} \rho(z) \left(1, z, z^2, z^3, z^4, z^6\right) dz$.

3. A novel polygonal FG plate element

3.1 Construction of quadratic serendipity shape function

In PFEM, a given domain is discretized into arbitrary polygonal elements before the shape functions are constructed over each polygonal element. Recently, the quadratic serendipity shape functions, which are with vertices and the mid-point of each boundary edge, over general polygonal elements have gained increasing attention of many researchers. Rand et al. [55] have presented an outline of construction quadratic serendipity shape functions over arbitrary convex polygons. Then, Floater [58] has provided a construction of serendipity quadratic shape functions over a polygon with any number of nodes based on polygonal splines. In this study, the approach presented in [55] is considered in order to construct the quadratic serendipity shape over arbitrary convex polygons. Accordingly, there are four

essential steps related to this construction of quadratic serendipity shape functions, which briefly expressed and illustrated in Fig. 3.

• Step 1: The shape function ϕ_i associated with vertices of the polygonal element is set. In this study, the Wachspress coordinate is used to calculate these shape functions ϕ_i.

• Step 2: The pairwise products of generalized barycentric coordinates $\varphi_{ab} := \phi_a \phi_b$ are determined. A result of the construction leads to $n(n+1)/2$ functions in total including mid-edge nodes and nodes inside the polygonal element.

• Step 3: An appropriate linear transformation $\mathbf{T}$, which are exhaustively reported in [55], is applied to the pairwise products of generalized barycentric coordinates φ_{ab} and set of functions ξ_{ij} associated with vertices and mid-side nodes of the polygonal element. Note that there are only $2n$ functions ξ_{ij} are defined in this step which are indexed over vertices and edge midpoints of the polygon element.

• Step 4: In order to satisfy the Lagrangian property, which are known that each function takes the value 1 at its associated node and 0 at all other nodes, another linear transformation matrix $\overline{\mathbf{T}}$ [55] is used to convert ξ_{ij} into a basis ψ_{ij}.

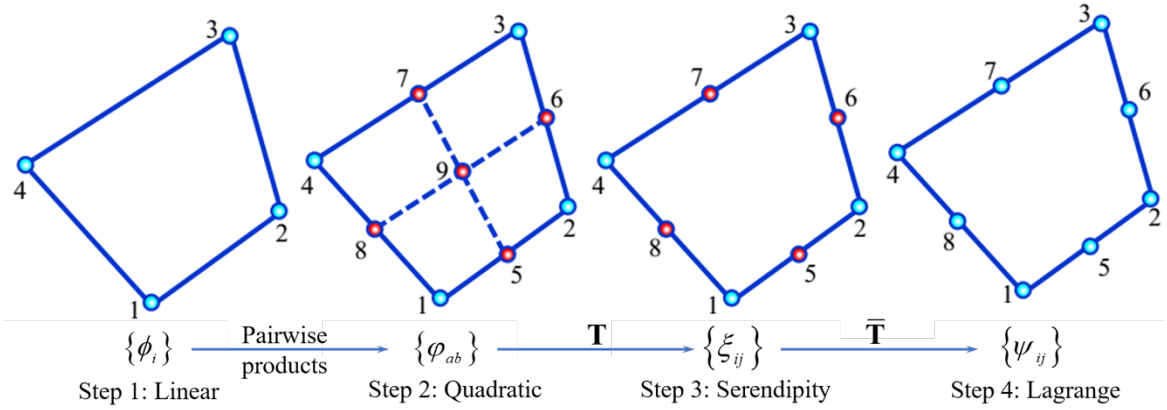

Fig. 3. Construction of quadratic serendipity shape functions.

For further a detail on this construction of quadratic serendipity shape functions for arbitrary polygon element, the interested readers are referred to [55]. Fig. 4 depicts the quadratic serendipity shape functions for a pentagonal element.

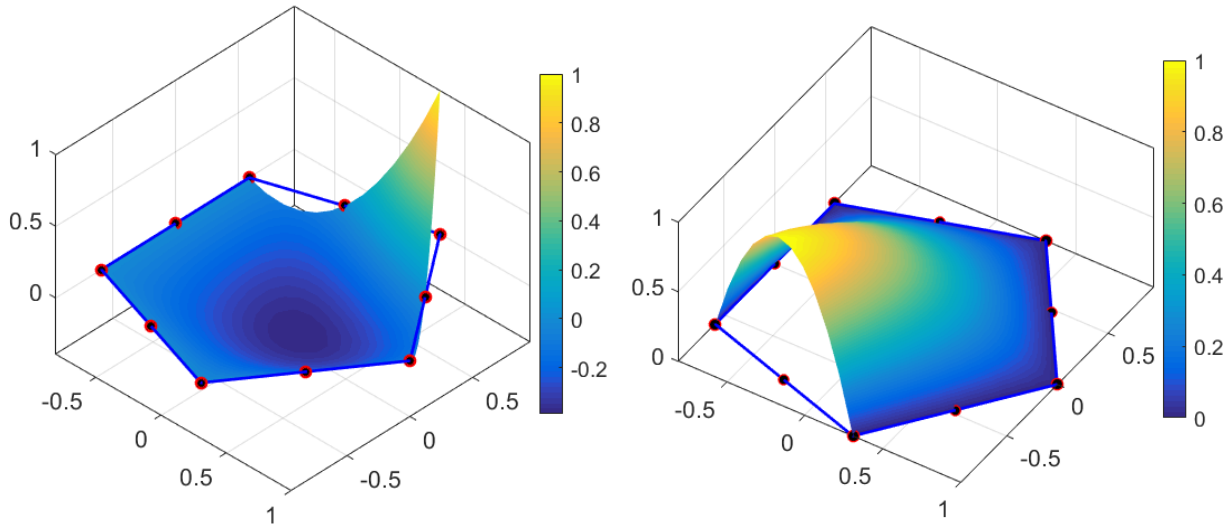

(a) (b)

Fig. 4. The quadratic serendipity shape functions for a pentagonal element

(a) Vertex node; (b) mid-side node.

3.2 PFEM formulation for FG plates

The physical domain Ω is decomposed into approximate Ω^h including non-overlapping polygonal elements. The primeval mesh Θ contains n_e elements and n_n nodes, such that $\Omega \approx \Omega^h = \sum_{e=1}^{n_e} \Omega^e$. Let $\boldsymbol{\phi}$ be the nodal basis (shape functions) of polygonal element Ω^e. Herein, the finite element solution $\mathbf{u}^h(\mathbf{x})$ of the displacement model for FGM plates can be expressed as

$$\mathbf{u}^h(\mathbf{x}) = \sum_{I}^{n_{ne}} \phi_I \mathbf{I}_7 \mathbf{d}_I = \sum_{I}^{n_{ne}} \boldsymbol{\phi}_I \mathbf{d}_I, \quad \text{in } \Omega^e, \tag{15}$$

where n_{ne} is the number of vertices of the polygonal element, $\mathbf{I}_7$ is the unit matrix of 7th rank, $\mathbf{d}_I = \left\{u_I, v_I, w_I, \beta_{xI}, \beta_{yI}, \phi_{xI}, \phi_{yI}\right\}^T$ denotes the displacement vector of the nodal degrees of freedom of $\mathbf{u}(\mathbf{x})$ associated with the Ith vertex of the polygonal element; and ϕ_I is the shape function at the Ith vertex of polygonal element.

Based on the approximation in Eq. (15), the strain components including the membrane, bending and shear strains in Eqs. (7) and (9) can be rewritten in compact forms as

$$\begin{aligned}
&\boldsymbol{\varepsilon}_0^L = \sum_I^{n_{ne}} \mathbf{B}_I^m \mathbf{d}_I, \quad \boldsymbol{\kappa}_1 = \sum_I^{n_{ne}} \mathbf{B}_I^{b1} \mathbf{d}_I, \quad \boldsymbol{\kappa}_2 = \sum_I^{n_{ne}} \mathbf{B}_I^{b2} \mathbf{d}_I, \\
&\boldsymbol{\varepsilon}_s = \sum_I^{n_{ne}} \mathbf{B}_I^{s0} \mathbf{d}_I, \quad \boldsymbol{\kappa}_s = \sum_I^{n_{ne}} \mathbf{B}_I^{s1} \mathbf{d}_I, \quad \boldsymbol{\varepsilon}_0^{NL} = \frac{1}{2} \sum_I^{n_{ne}} \mathbf{B}_I^{mNL} \mathbf{d}_I,
\end{aligned} \tag{16}$$

where

$$\begin{aligned}
&\mathbf{B}_I^m = \begin{bmatrix} \phi_{I,x} & 0 & 0 & 0 & 0 & 0 & 0 \\ 0 & \phi_{I,y} & 0 & 0 & 0 & 0 & 0 \\ \phi_{I,y} & \phi_{I,x} & 0 & 0 & 0 & 0 & 0 \end{bmatrix}, \quad \mathbf{B}_I^{b1} = \begin{bmatrix} 0 & 0 & 0 & \phi_{I,x} & 0 & 0 & 0 \\ 0 & 0 & 0 & 0 & \phi_{I,y} & 0 & 0 \\ 0 & 0 & 0 & \phi_{I,y} & \phi_{I,x} & 0 & 0 \end{bmatrix}, \\
&\mathbf{B}_I^{s0} = \begin{bmatrix} 0 & 0 & \phi_{I,x} & \phi_I & 0 & 0 & 0 \\ 0 & 0 & \phi_{I,y} & 0 & \phi_I & 0 & 0 \end{bmatrix}, \quad \mathbf{B}_I^{b2} = c \begin{bmatrix} 0 & 0 & 0 & \phi_{I,x} & 0 & \phi_{I,x} & 0 \\ 0 & 0 & 0 & 0 & \phi_{I,y} & 0 & \phi_{I,y} \\ 0 & 0 & 0 & \phi_{I,y} & \phi_{I,x} & \phi_{I,y} & \phi_{I,x} \end{bmatrix}, \\
&\mathbf{B}_I^{s1} = 3c \begin{bmatrix} 0 & 0 & 0 & \phi_I & 0 & \phi_I & 0 \\ 0 & 0 & 0 & 0 & \phi_I & 0 & \phi_I \end{bmatrix}, \quad \mathbf{B}_I^{mNL} = \mathbf{H}\boldsymbol{\Lambda}.
\end{aligned} \tag{17}$$

where $\phi_{I,x}$ and $\phi_{I,y}$ are the derivatives of the shape functions ϕ_I with respect to x and y, respectively. The matrices $\mathbf{H}$ and $\boldsymbol{\Lambda}$ are expressed by

$$\mathbf{H} = \begin{bmatrix} w_{0,x} & 0 \\ 0 & w_{0,y} \\ w_{0,y} & w_{0,x} \end{bmatrix}, \quad \boldsymbol{\Lambda} = \begin{bmatrix} 0 & 0 & \phi_{I,x} & 0 & 0 & 0 & 0 \\ 0 & 0 & \phi_{I,y} & 0 & 0 & 0 & 0 \end{bmatrix}. \tag{18}$$

Now, substituting Eq. (16) into Eq. (10), the governing algebraic equations of the FG plate using in PFEM for nonlinear analysis can be expressed in the following form

$$\mathbf{K}(\mathbf{d})\mathbf{d} = \mathbf{F}, \tag{19}$$

in which $\mathbf{K}(\mathbf{d})$ is the global stiffness matrix which can be computed as

$$\mathbf{K}(\mathbf{d}) = \mathbf{K}_L + \mathbf{K}_{NL}(\mathbf{d}) + \mathbf{K}_G, \tag{20}$$

in which $\mathbf{K}_L$, $\mathbf{K}_{NL}$ and $\mathbf{K}_G$ are the global linear stiffness matrix, the global nonlinear stiffness matrix and the global geometric stiffness matrix, respectively. These global matrices are

respectively assembled from the element matrices $\mathbf{K}_L^e, \mathbf{K}_{NL}^e$ and $\mathbf{K}_G^e$ of the element Ω^e, which can be defined as follows

$$\begin{aligned}
\mathbf{K}_L^e &= \int_{\Omega_e} \left(\mathbf{B}_I\right)^T \mathbf{D}^* \mathbf{B}_I d\Omega + \int_{\Omega_e} \left(\mathbf{S}_I\right)^T \mathbf{D}_s^* \mathbf{S}_I d\Omega_e, \\
\mathbf{K}_{NL}^e &= \int_{\Omega_e} \left(\frac{1}{2} \left(\mathbf{B}_I^L\right)^T \mathbf{D}^{**} \mathbf{B}_I^L + \left(\mathbf{B}_I^{NL}\right)^T \mathbf{D}^{**} \mathbf{B}_I^L + \frac{1}{2} \left(\mathbf{B}_I^{NL}\right)^T \mathbf{D}^{**} \mathbf{B}_I^{NL} \right) d\Omega_e, \\
\mathbf{K}_G^e &= \int_{\Omega_e} \left(\mathbf{\Lambda}_I\right)^T \bar{\mathbf{N}} \mathbf{\Lambda}_I d\Omega_e,
\end{aligned} \tag{21}$$

in which the matrices $\mathbf{B}_I, \mathbf{S}_I, \mathbf{B}_I^L$ and $\mathbf{B}_I^{NL}$ are defined by

$$\mathbf{B}_I = \begin{bmatrix} \mathbf{B}_I^m & \mathbf{B}_I^{b1} & \mathbf{B}_I^{b2} \end{bmatrix}^T, \quad \mathbf{S}_I = \begin{bmatrix} \mathbf{B}_I^{s0} & \mathbf{B}_I^{s1} \end{bmatrix}^T, \tag{22}$$

$$\mathbf{B}_I^L = \begin{bmatrix} \mathbf{B}_I & \mathbf{S}_I \end{bmatrix}^T, \quad \mathbf{B}_I^{NL} = \begin{bmatrix} \mathbf{B}_I^{mNL} & \mathbf{0} \end{bmatrix}^T, \tag{23}$$

and $\mathbf{D}^{**}$ is given by

$$\mathbf{D}^{**} = \begin{bmatrix} \mathbf{D}^* & \mathbf{0} \\ \mathbf{0} & \mathbf{D}_s^* \end{bmatrix}. \tag{24}$$

The in-plane traction matrix is defined by

$$\bar{\mathbf{N}} = \begin{bmatrix} \bar{N}_x & \bar{N}_{xy} \\ \bar{N}_{xy} & \bar{N}_y \end{bmatrix}, \tag{25}$$

where $\left\{\bar{N}_x, \bar{N}_y, \bar{N}_{xy}\right\} = \int_{-h/2}^{h/2} \left\{\sigma_x, \sigma_y, \sigma_{xy}\right\} dz.$

The global load vector $\mathbf{F}$ is expressed by

$$\mathbf{F} = \int_{\Omega} q \boldsymbol{\phi} \mathrm{d}\Omega + \mathbf{f}^b, \tag{26}$$

in which $\mathbf{f}^b$ is the complementary term of $\mathbf{F}$ subjected to prescribed boundary loads.

For the transient analysis problem, finite element formulation yields

$$\mathbf{K}\mathbf{d} + \mathbf{M}\ddot{\mathbf{d}} = \mathbf{F}, \tag{27}$$

where $\mathbf{M}$ denotes the global mass matrix, which can be expressed as follows:

$$\mathbf{M} = \int_{\Omega} \boldsymbol{\phi}^T \mathbf{m} \boldsymbol{\phi} d\Omega. \tag{28}$$

It is well known that the shear locking phenomenon will appear when the plate's thickness becomes smaller. To avoid this shortcoming, a shear locking free polygonal FG plate element approach based on an assumed strain field via the Timoshenko's beam formulae is addressed. This approach will be presented in the next subsection.

3.3 Locking-free polygonal FG plate element

3.3.1 Deformation of the Timoshenko's beam element

Considering a Timoshenko's thick beam element as shown in Fig. 5, the deflection $w(\xi)$, rotation $\beta(\xi)$ and shear strain $\gamma(\xi)$ of the thick beam element which based on the Timoshenko's beam theory are correspondingly expressed as follows [61, 62]

$$\begin{aligned} w(\xi) &= w_i(1-\xi) + w_j\xi + \frac{l}{2}\left(-\beta_i + \beta_j\right)\xi(1-\xi) - \frac{l}{2}\Gamma(1-2\Im)\xi(1-\xi)(1-2\xi), \\ \beta(\xi) &= \beta_i(1-\xi) + \beta_j\xi - 3\Gamma(1-2\Im)\xi(1-\xi), \\ \gamma(\xi) &= \Im\Gamma, \end{aligned} \tag{29}$$

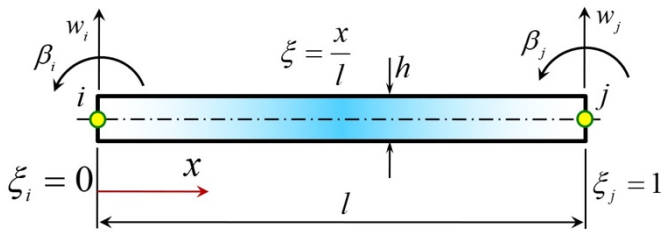

Fig. 5. Timoshenko beam element.

in which

$$\Gamma = \frac{2}{l}\left(-w_i + w_j\right) + \beta_i + \beta_j, \quad \Im = \frac{6\lambda}{1+12\lambda}, \quad \lambda = \frac{D^b}{D^s l^2}, \tag{30}$$

with D^b, D^s and l represent the bending, shear stiffness constants and length of the beam element, respectively. It is seen that when the thickness h of the plate approaches zeros, λ in Eq. (30) will tend to zeros ($\lim_{h\to 0}\lambda = \frac{1}{l^2}\lim_{h\to 0}\frac{D^b}{D^s} = 0$). Therefore, $\Im$ will also go toward zeros. As a result, the transverse shear strain $\gamma(\xi)$ will be eliminated automatically. Consequently, shear

locking issue of the interpolation can be suppressed based on the Timoshenko's beam theory. Now, this theory is extended for FG plate polygonal elements.

3.3.2 An approximation of assumed shear strains

Considering an FG plate polygonal element Ω^e with the edges number $n \geq 3$, which has the normal and tangential directions of each edge is described in Fig. 6, the generalized nodal displacement of the polygonal element can be placed in the following vector

$$\mathbf{d}^e = \{\mathbf{d}_1, \mathbf{d}_2, \ldots, \mathbf{d}_{n-1}, \mathbf{d}_n\}^T, \tag{31}$$

where $\mathbf{d}_i = \{u_i, v_i, w_i, \beta_{xi}, \beta_{yi}, \phi_{xi}, \phi_{yi}\}^T$ with $(i = 1, 2, ..., n-1, n)$. Adopting the same approach [61], Nguyen-Xuan [46] devised the interpolation procedure for shear strain fields along the polygonal element edges based on Timoshenko's beam theory. Accordingly, the assumed shear strains of the polygonal element can be written in the matrix form as follows

$$\hat{\boldsymbol{\gamma}}^e = \tilde{\mathbf{S}}^e \mathbf{d}^e = \left[\tilde{\mathbf{B}}^{s0}, \mathbf{B}^{s1}\right]\{\mathbf{d}\}^e, \tag{32}$$

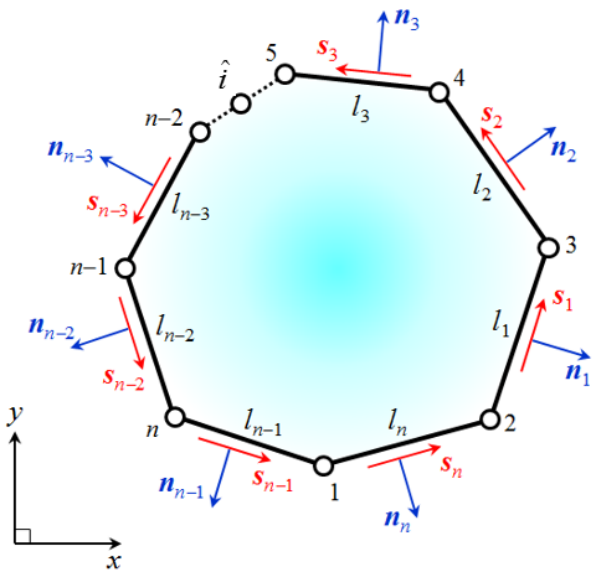

Fig. 6. The normal and tangential direction of each edge of polygonal element.

in which the matrix $\mathbf{B}^{s1}$ is presented in Eq. (17). And the matrix $\tilde{\mathbf{B}}^{s0} = \left[\mathbf{H}^s\right]\left[\mathbf{I}^s\right]\left[\mathbf{G}^s\right]$ with $\left[\mathbf{H}^s\right], \left[\mathbf{I}^s\right]$ and $\left[\mathbf{G}^s\right]$ can be expressed as, respectively

$$\left[\mathbf{H}^s\right]_{\{2\times n\}} = \sum_{\hat{i},\hat{j},\hat{k},\hat{m}} \begin{bmatrix} \dfrac{b_{\hat{m}}\phi_{\hat{j}}}{c_{\hat{i}}b_{\hat{m}} - c_{\hat{m}}b_{\hat{i}}} - \dfrac{b_{\hat{j}}\phi_{\hat{k}}}{c_{\hat{j}}b_{\hat{i}} - c_{\hat{i}}b_{\hat{j}}} \\ \dfrac{c_{\hat{m}}\phi_{\hat{j}}}{c_{\hat{i}}b_{\hat{m}} - c_{\hat{m}}b_{\hat{i}}} - \dfrac{c_{\hat{j}}\phi_{\hat{k}}}{c_{\hat{j}}b_{\hat{i}} - c_{\hat{i}}b_{\hat{j}}} \end{bmatrix}, \tag{33}$$

$$\left[\mathbf{I}^s\right]_{\{n\times n\}} = \left[\delta_{\hat{i}\hat{i}}\Im_{\hat{i}}\right], \tag{34}$$

$$\left[\mathbf{G}^s\right]_{\{n,7n\}} = \sum_{\hat{i},\hat{j}}\left[-2_{\hat{i},7\hat{j}-4}, c_{\hat{i},7\hat{j}-3}, -b_{\hat{i},7\hat{j}-2}\right] + \sum_{\hat{i},\hat{k}}\left[2_{\hat{i},7\hat{k}-4}, c_{\hat{i},7\hat{k}-3}, -b_{\hat{i},7\hat{k}-2}\right], \tag{35}$$

where $\Im_{\hat{i}}$ is presented in Eq. (30). Note that $\phi_{\hat{i}}$ is the Wachspress shape function at the $\hat{i}$th vertex of polygonal element Ω^e and

$$\left\{b_{\hat{i}} = y_{\hat{j}} - y_{\hat{k}},\ c_{\hat{i}} = x_{\hat{k}} - x_{\hat{j}}\right\} \ \text{ with } \begin{cases} \hat{i} = 1,2,\ldots,\mathrm{n}-2,\mathrm{n}-1,n; \quad \hat{j} = 2,3,\ldots,n-1,\mathrm{n},1; \\ \hat{k} = 3,4,\ldots,n,1,2; \quad \hat{m} = n,1,\ldots n-2,n-1. \end{cases} \tag{36}$$

3.3.3 A novel approximation of assumed bending strains

In this study, the assumed bending strains of the arbitrary polygonal element using serendipity shape functions ψ is firstly presented based on the work of Soh et al. [62], which only were applied for triangular and quadrilateral elements. Accordingly, these strains can be expressed in the following compact form

$$\hat{\boldsymbol{\varepsilon}}^e = \tilde{\mathbf{B}}^e\mathbf{d}^e = \left[\mathbf{B}^m, \tilde{\mathbf{B}}^{b1}, \mathbf{B}^{b2}\right]\left\{\mathbf{d}\right\}^e, \tag{37}$$

where $\tilde{\mathbf{B}}^{b1} = \mathbf{B}_1^{b1} + \hat{\mathbf{B}}_1^{b1}$. The matrices $\mathbf{B}^m, \mathbf{B}^{b1}$ and $\mathbf{B}^{b2}$ can be found in Eq. (17). Meanwhile, $\hat{\mathbf{B}}^{b1} = \left[\mathbf{H}_1^b\right]\left[\mathbf{G}_1^b\right] + \left[\mathbf{H}_2^b\right]\left[\mathbf{G}_2^b\right]$ with the matrices $\left[\mathbf{H}_1^b\right], \left[\mathbf{H}_2^b\right], \left[\mathbf{G}_1^b\right]$ and $\left[\mathbf{G}_2^b\right]$ are defined as, respectively

$$\left[\mathbf{H}_1^b\right]_{\{3xn\}} = \left[\frac{\partial\psi_{\bar{j}}}{\partial x}, 0, \frac{\partial\psi_{\bar{j}}}{\partial y}\right]^T, \quad \left[\mathbf{H}_2^b\right]_{\{3xn\}} = \left[0, \frac{\partial\psi_{\bar{j}}}{\partial y}, \frac{\partial\psi_{\bar{j}}}{\partial x}\right]^T, \tag{38}$$

$$\left[\mathbf{G}_1^b\right]_{\{n,7n\}} = \sum_{\hat{i},\hat{j}}\left[\tilde{g}^1_{\hat{i},7\hat{j}-4}, \tilde{g}^2_{\hat{i},7\hat{j}-3}, \tilde{g}^3_{\hat{i},7\hat{j}-2}\right] + \sum_{\hat{i},\hat{k}}\left[-\tilde{g}^1_{\hat{i},7\hat{k}-4}, \tilde{g}^2_{\hat{i},7\hat{k}-3}, \tilde{g}^3_{\hat{i},7\hat{k}-2}\right], \tag{39}$$

$$\left[\mathbf{G}_2^b\right]_{\{n,7n\}} = \sum_{\hat{i},\hat{j}}\left[\hat{g}^1_{\hat{i},7\hat{j}-4}, \hat{g}^2_{\hat{i},7\hat{j}-3}, \hat{g}^3_{\hat{i},7\hat{j}-2}\right] + \sum_{\hat{i},\hat{k}}\left[-\hat{g}^1_{\hat{i},7\hat{k}-4}, \hat{g}^2_{\hat{i},7\hat{k}-3}, \hat{g}^3_{\hat{i},7\hat{k}-2}\right], \tag{40}$$

in which $\bar{j} = n+1, n+2, \cdots, 2n-1, 2n.$ And

$$\begin{aligned}
&\tilde{g}^1_{\hat{i}} = \frac{3c_{\hat{i}}\left(1-2\delta_{\hat{i}}\right)}{2l^2_{\hat{i}}}; \quad \tilde{g}^2_{\hat{i}} = \frac{b^2_{\hat{i}} - 0.5c^2_{\hat{i}}\left(1-6\delta_{\hat{i}}\right)}{2l^2_{\hat{i}}}; \quad \tilde{g}^3_{\hat{i}} = \frac{3b_{\hat{i}}c_{\hat{i}}\left(1-2\delta_{\hat{i}}\right)}{4l^2_{\hat{i}}}, \\
&\hat{g}^1_{\hat{i}} = \frac{-3b_{\hat{i}}\left(1-2\delta_{\hat{i}}\right)}{2l^2_{\hat{i}}}; \quad \hat{g}^2_{\hat{i}} = \frac{3b_{\hat{i}}c_{\hat{i}}\left(1-2\delta_{\hat{i}}\right)}{4l^2_{\hat{i}}}; \quad \hat{g}^3_{\hat{i}} = \frac{c^2_{\hat{i}} - 0.5b^2_{\hat{i}}\left(1-6\delta_{\hat{i}}\right)}{2l^2_{\hat{i}}},
\end{aligned} \tag{41}$$

where $l_{\hat{i}} = \left\|\boldsymbol{x}_{\hat{j}} - \boldsymbol{x}_{\hat{k}}\right\|$ denotes the length of the $\hat{i}$th edge of polygonal element and $\hat{i}, \hat{j}, \hat{k}$ is presented in Eq. (36). It is noted that although the quadratic serendipity shape functions, which is added mid-nodes on the edges are employed in this study, the number of DOFs per polygonal element does not increase.

3.4 Nonlinear analysis

In this study, the Newton-Rapshon procedure [64, 74] is utilized to solve the nonlinear equation in Eq. (19). These iterations, in which the solutions in the current step are derived from the solutions of previous step, are repeated until the solution converges. For the nonlinear transient analysis of FG plates, which the equations of dynamic are dependent on both unknown displacements and time domain, a combination the Newmark's integration scheme [65] and Picard methods is adopted in this study. Following this flow chart, at the initial time $t = 0,$ values of displacement $\mathbf{d}$, velocity $\dot{\mathbf{d}}$ and acceleration $\ddot{\mathbf{d}}$ are prescribed to be zeros. When the displacement at time $t = \left(i+1\right)\Delta t$ is obtained, the velocities and accelerations, which is first and second derivatives of displacement at this step can be defined as

$$\begin{aligned}
\ddot{\mathbf{d}}_{i+1} &= \frac{1}{\beta\left(\Delta t\right)^2}\left(\mathbf{d}_{i+1} - \mathbf{d}_i\right) - \frac{1}{\beta\Delta t}\dot{\mathbf{d}}_i - \left(\frac{1}{2\beta} - 1\right)\ddot{\mathbf{d}}_i, \\
\dot{\mathbf{d}}_{i+1} &= \dot{\mathbf{d}}_i + \Delta t\left(1-\gamma\right)\ddot{\mathbf{d}}_i + \gamma\Delta t\ddot{\mathbf{d}}_{i+1},
\end{aligned} \tag{42}$$

where the values of $\gamma = 0.5$ and $\beta = 0.25$ following the average acceleration scheme [67]. Now, substituting Eq. (42) into Eq. (27), the following equation can be rewritten as follows

$$\hat{\mathbf{K}}_{i+1}\mathbf{d}_{i+1} = \hat{\mathbf{F}}_{i+1}, \tag{43}$$

where

$$\begin{aligned}
\hat{\mathbf{K}}_{i+1} &= \mathbf{K}_{i+1} + \frac{1}{\beta\left(\Delta t\right)^2}\mathbf{M}, \\
\hat{\mathbf{F}}_{i+1} &= \mathbf{F}_{i+1} + \mathbf{M}\left[\frac{1}{\beta\left(\Delta t\right)^2}\mathbf{d}_i + \frac{1}{\beta\Delta t}\dot{\mathbf{d}}_i + \left(\frac{1}{2\beta} - 1\right)\ddot{\mathbf{d}}_i\right].
\end{aligned} \tag{44}$$

It should be noted that in Eq. (43), all parameters are known from the previous solutions, i.e. $t = i\Delta t$, except the nonlinearly stiffness matrix $\mathbf{K}_{i+1}$, which depends on the displacements $\mathbf{d}_{i+1}$. Therefore, the Picard method is employed to re-approximate Eq. (43), which can be written as follows

$$\hat{\mathbf{K}}\left(\mathbf{d}_{i+1}^{j}\right)\mathbf{d}_{i+1}^{j+1} = \hat{\mathbf{F}}_{i+1}, \tag{45}$$

in which j is the number of iterations. Eq. (45) is iteratively solved until the error of the displacement is satisfied.

4. Numerical examples

In this section, various numerical examples are investigated to demonstrate the accuracy and stability of the proposed approach and the obtained results are compared to other published ones in the literature. Unless mentioned otherwise, the material properties of FG plates which are employed in all examples are estimated following the rule of mixtures. Numerical examples have been carried out for perfect FG plates including both static and dynamic problems before extending for porous FG plate with various porosity distributions and porosity volume fractions.

4.1 Convergence and verification studies

Firstly, to evaluate the validity and the convergence of the proposed approach, the model of an isotropic square plate under uniform load $q = 1$ with fully simply supported (SSSS) boundary condition will be investigated. The plate has length a and the thickness h. The elastic material properties are: Young's modulus $E = 1,092,000$ and Poisson's ratio $\nu = 0.3$. Owing to the symmetric properties, only the lower-left corner of square plate is considered. The square plate domain is then discretized using n-node polygonal element with four meshes level as depicted Fig. 7. The normalized of deflection and moment at the central of the square plate are defined $\bar{w} = 100Dw_c / qa^4$ and $\bar{M} = 100DM_c / qa^2$, respectively with $D = Eh^3 / \left(12\left(1-\nu^2\right)\right)$. Fig. 8 shows the convergence of the normalized central deflection and moment of SSSS boundary conditions with ratio $a / h = 1000$. The present results are then compared with those of the well-known MITC4 element and those reported in [46] including polygonal Reissner–Mindlin plate element based on Wachspress shape functions (PRMn-W) and piecewise-linear shape functions (PRMn-PL), respectively. It can be seen that the obtained results converge well for both deflection and moment which the analytical solutions are found in [68]. General speaking, the proposed formulation based on the quadratic serendipity shape functions shows more accurate results in comparison with the others.

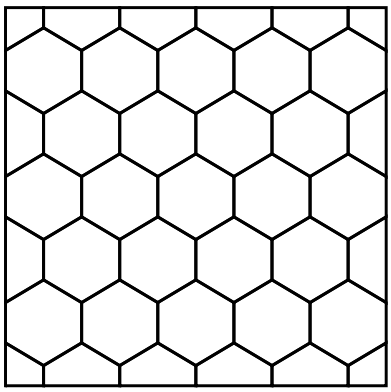

1st mesh

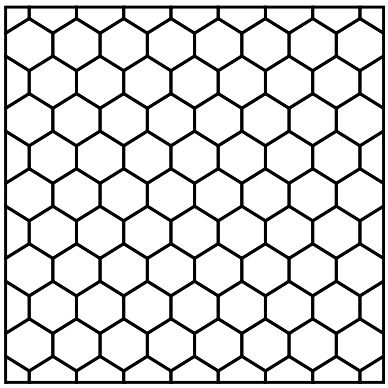

2nd mesh

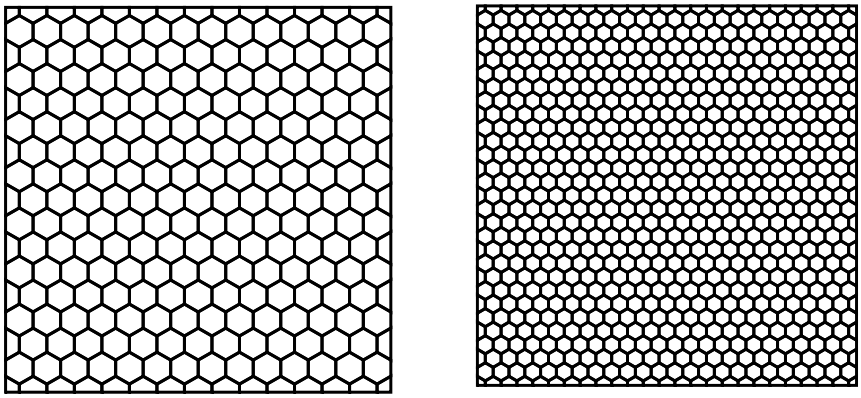

3rd mesh 4th mesh

Fig. 7. Polygonal meshes of a square plate.

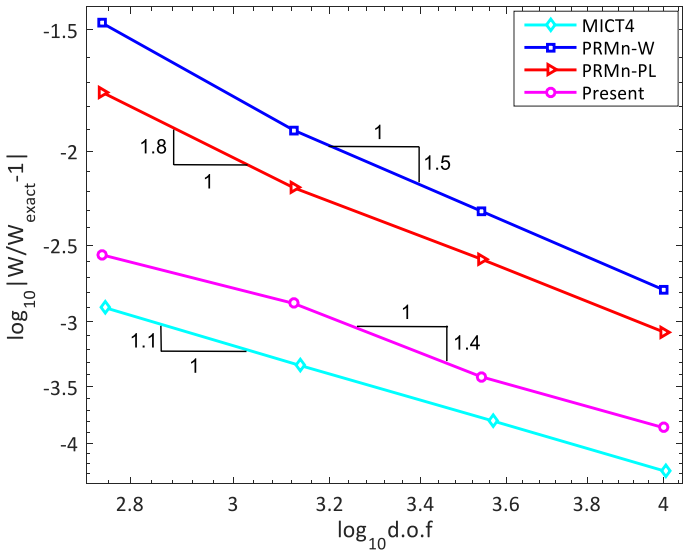

(a)

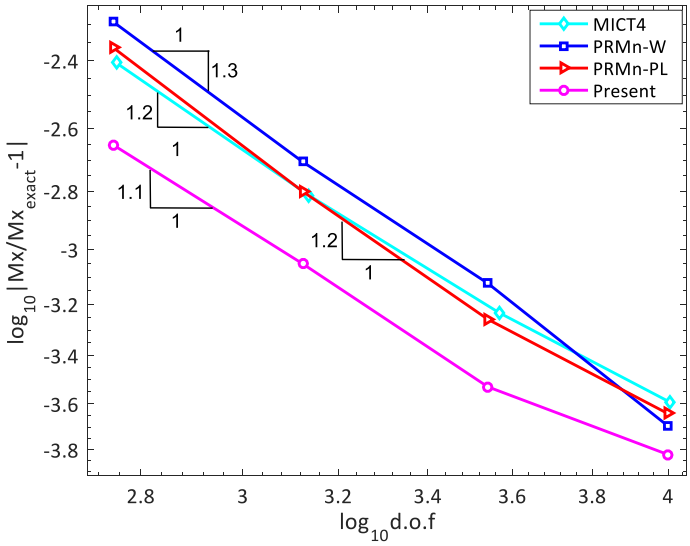

(b)

Fig. 8. The convergence of a SSSS plate with ratio $a/h=1000$.

(a) central deflection; (b) central moment.

Next, in order to investigate the effect of mesh distortion on the numerical results, distorted *n*-node polygonal meshes as shown in Fig. 9 with distorted factor $s \in [0,1]$ [69] are investigated. The results the central deflection versus with the distorted factors for a thin plate with ratio $a/h = 1000$ are illustrated in Fig. 10. It is observed that the proposed element always gives accurate and stable results when the meshes are highly distorted. Furthermore, the computational efficiency of the proposed formulation is compared with the others including PRMn-W and PRMn-PL which are reported by Nguyen-Xuan [46]. Fig. 11 illustrates the CPU time for setting up the global stiffness matrix and solving system equation of a SSSS FG square plate versus DOFs. The results are compiled by a personal computer with Intel(R) Core(TM) i5-7200U, CPU – 2.5 GHz and RAM - 8 GB.

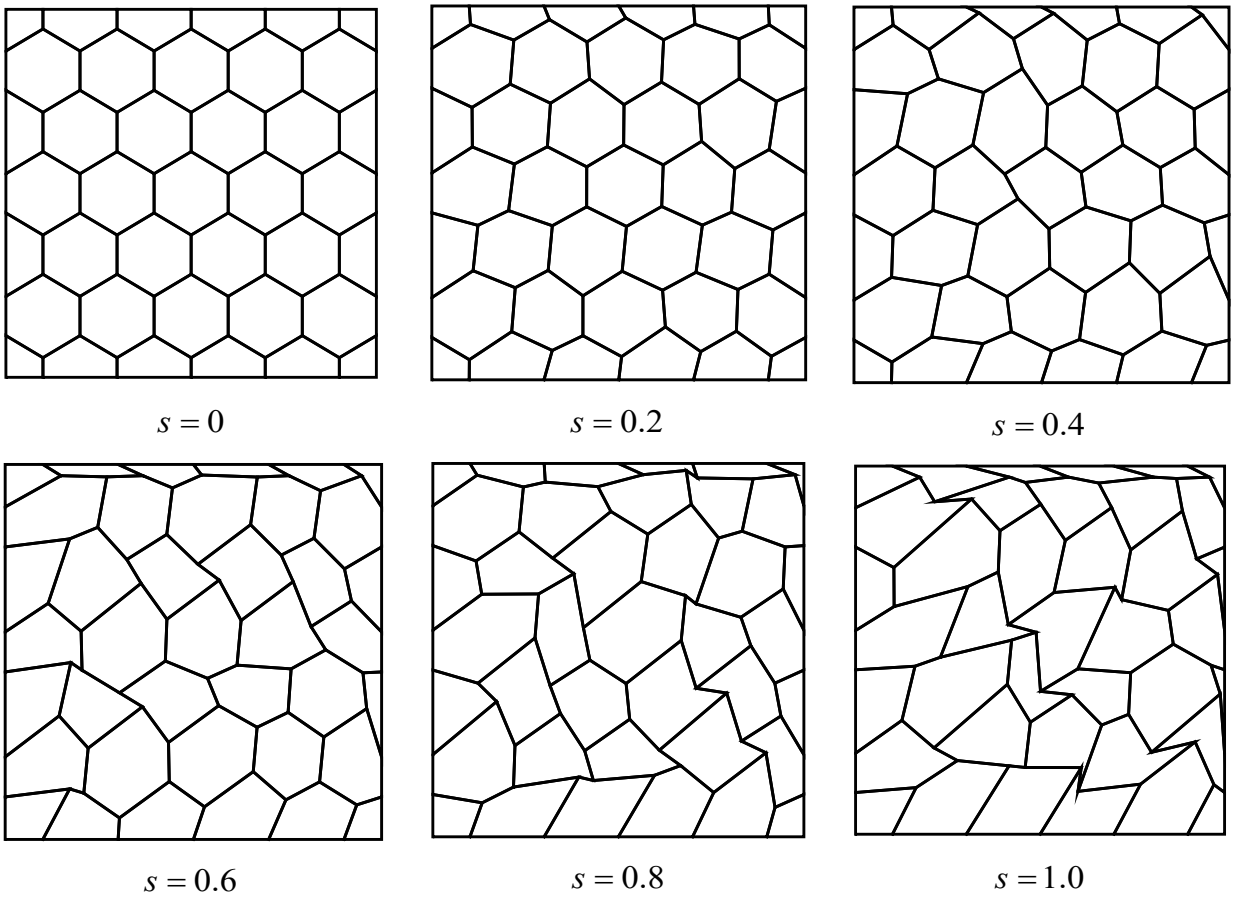

Fig. 9. Distorted polygonal meshes of square plate with distorted factors $s = 0; 0.2; 0.4; 0.6; 0.8; 1.0$

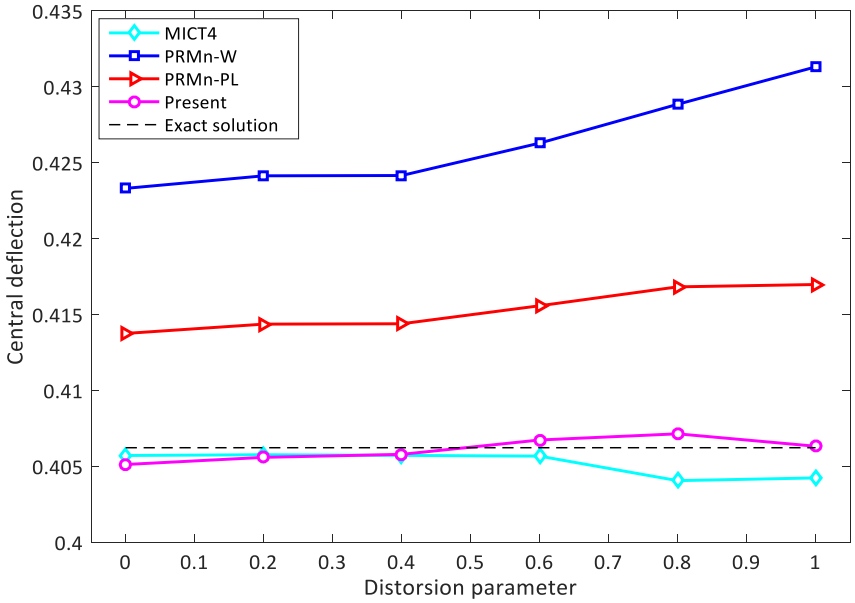

Fig. 10. The effects of distorted mesh on the central deflection of a SSSS plate.

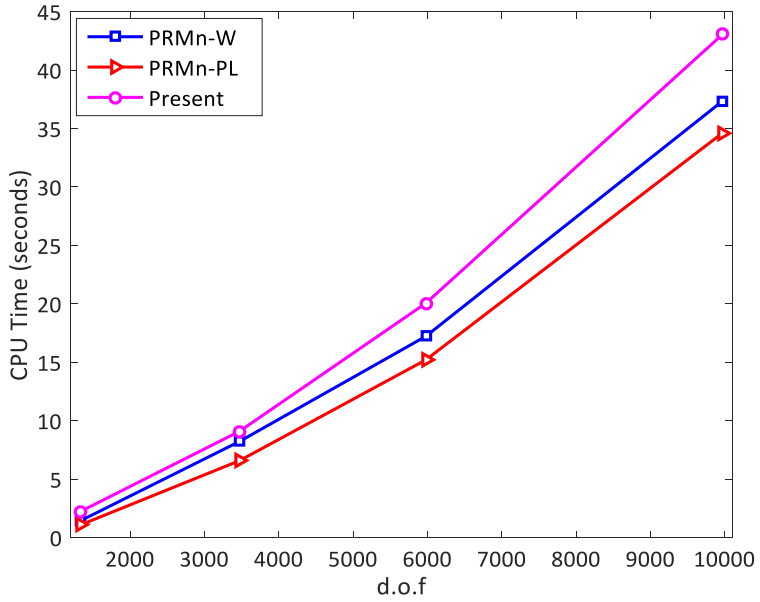

Fig. 11. CPU times for setting up the global stiffness matrix and solving system equations of a SSSS FG plate.

Finally, the robustness of the proposed method is further demonstrated for complicated domain geometries in Fig. 12a. The complicated plate domain which has thickness $h = 0.5$ and under uniform load $p = 1$ is discretized into n-node polygonal elements as shown in Fig. 12b. The deflection and moment of central point in x-direction against the increase in levels of meshes and DOFs for thin plate is illustrated in Fig. 13, respectively. A reference solution of this example can be found in [46], which was obtained based on a fine mesh using four-node MITC4 elements. As can be seen that the proposed formulation using the serendipity shape

functions performs far better than PRMn-W and PRMn-PL elements, respectively, which is reported in [46]. The above numerical results verify the accuracy and reliability of the proposed formulations.

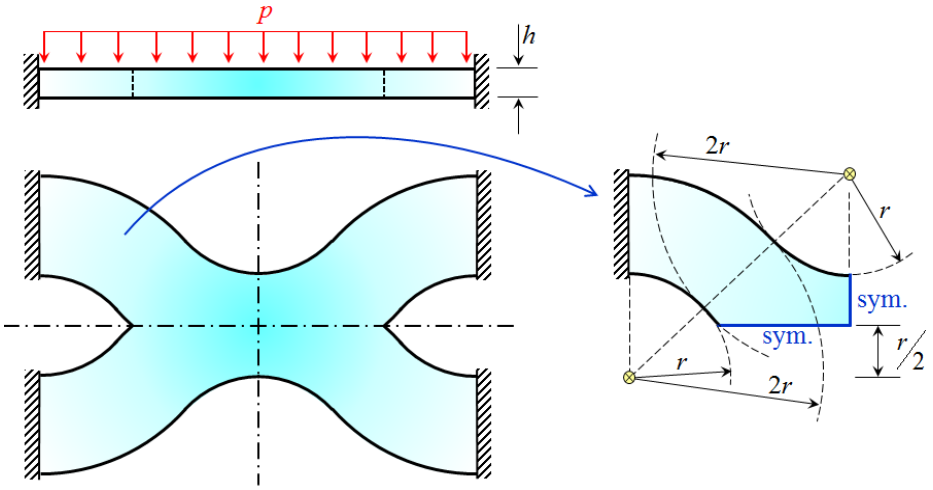

a)

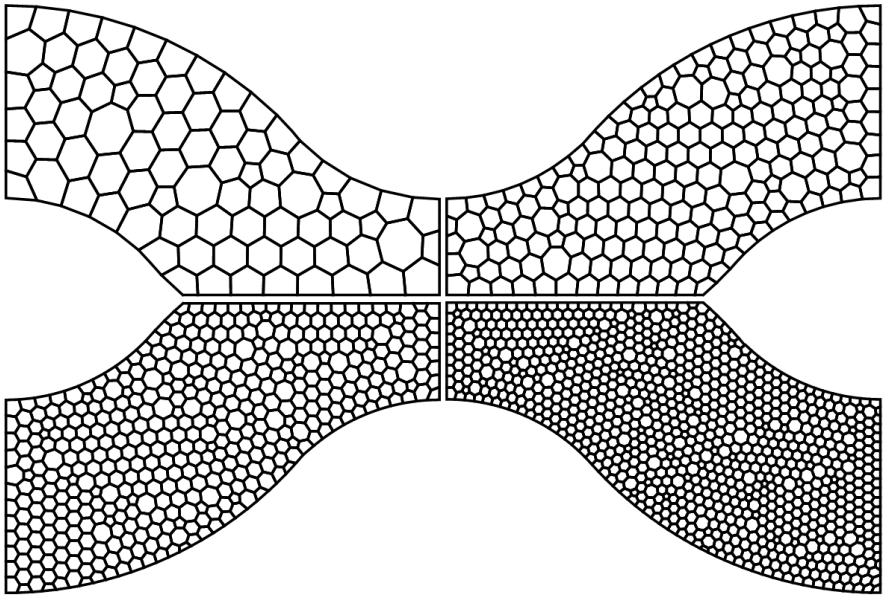

b)

Fig. 12. Model and polygonal mesh of a plate with complicated shape.

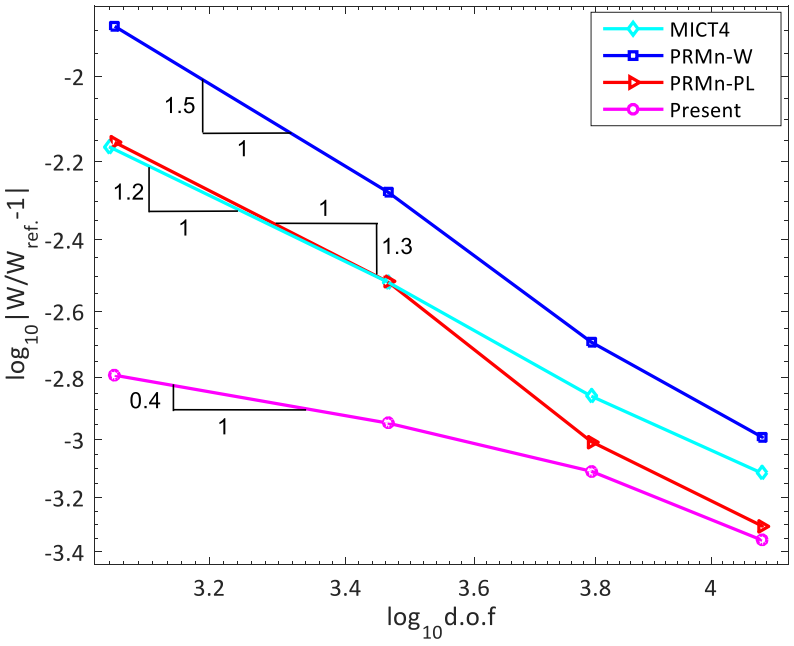

(a)

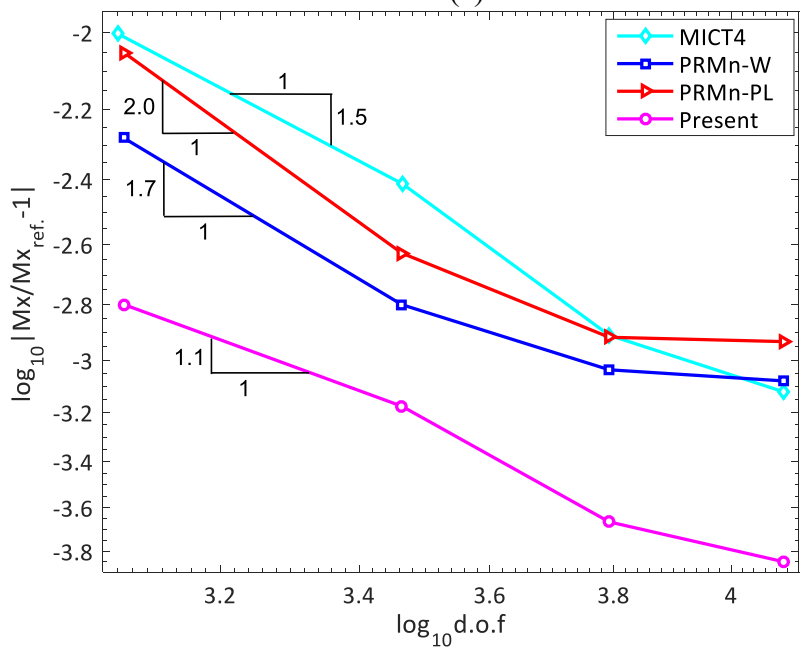

(b)

Fig. 13. The convergence of a plate with complicated shape

(a) central deflection and (b) central moment.

4.2 Static analysis of FG plates

4.2.1 Linear analysis

The static bending analysis of perfect FG plates will be investigated in this section. Table 1 shows the properties of the FG materials which will be used throughout the examples. A SSSS FG square plate which is made of alumina and aluminum (Al/Al_2O_3) is considered to

study the effects of ratio a/h and material index n on the numerical results. The plate is subjected to a distributed sinusoidal load which is defined as $q = q_0 \sin(\pi x/a)\sin(\pi y/a)$, as depicted in Fig. 14. The normalized deflection and axial stress at the central of the plate are defined by $\bar{w} = 10wE_c h^3/(q_0 a^4)$ and $\bar{\sigma}_{xx} = \bar{\sigma} h/(q_0 a^2)$, respectively. The results which are generated from the proposed approach are presented in Table 2 comparing with the Carrera's unified formulation by Carrera et al. [70], ES-MITC3 by Nguyen et al. [71], HSDT model is reported by Neves et al. [72]. As can be seen, the results which obtained from the proposed approach agree well with other reference values for all ratios a/h and material index n. In addition, Fig. 15 depicts the distribution of normalized axial and shear stresses through the thickness of perfect FG square plate under sinusoidal load with $a/h = 4$ and various material index n.

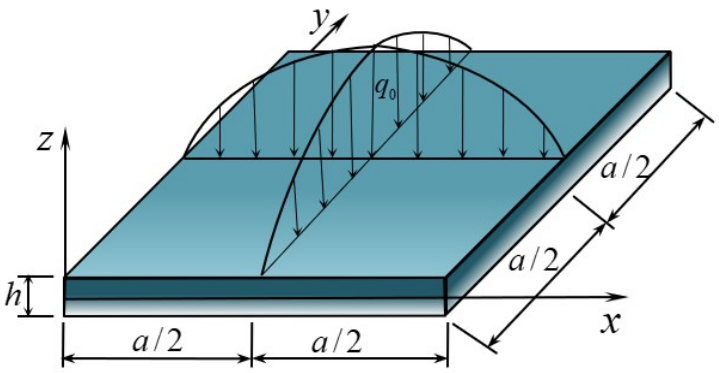

Fig. 14. A square FG plate subjected to sinusoidal load.

Table 1
Material properties of FG plates

Property	Material		
	Al	Al_2O_3	ZrO_2
E (GPa)	70	380	151
ν	0.3	0.3	0.3
ρ (kg/m^3)	2707	3800	3000

Table 2
Comparison of normalized central deflections $\bar{w}$ and axial stress $\bar{\sigma}_{xx}$ of SSSS Al/Al_2O_3 square plates under sinusoidal load.

n	Theory	$a/h=4$		$a/h=10$		$a/h=100$	
		$\bar{w}$	$\bar{\sigma}_{xx}$	$\bar{w}$	$\bar{\sigma}_{xx}$	$\bar{w}$	$\bar{\sigma}_{xx}$
1	Carrera et al. [70]	0.7289	0.7856	0.5890	2.0068	0.5625	20.149
	ES-MITC3 [71]	0.7271	0.5787	0.5874	1.4825	0.5609	14.894
	HSDT [72]	0.7308	0.5806	0.5913	1.4874	0.5648	14.944
	Present	0.7279	0.5811	0.5882	1.4896	0.5622	14.989
4	Carrera et al. [70]	1.1673	0.5986	0.8828	1.5874	0.8286	16.047
	ES-MITC3 [71]	1.1593	0.4390	0.8795	1.1719	0.8263	11.862
	HSDT [72]	1.1553	0.4338	0.877	1.1592	0.8241	11.737
	Present	1.1588	0.4391	0.8791	1.1757	0.8280	11.939
10	Carrera et al. [70]	1.3925	0.4345	1.0090	1.1807	0.9361	11.989
	ES-MITC3 [71]	1.3896	0.3220	1.0061	0.8730	0.9332	8.8566
	HSDT [72]	1.376	0.3112	0.9952	0.8468	0.9228	8.6011
	Present	1.3882	0.3218	1.0051	0.87581	0.9354	8.9198

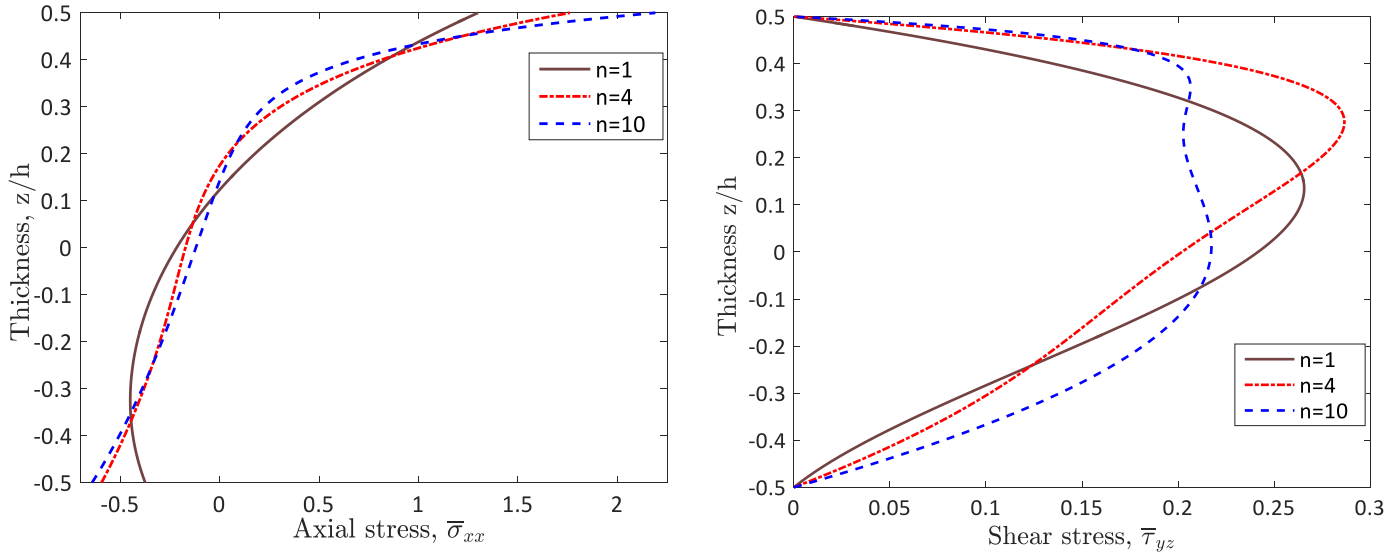

(a) (b)

Fig. 15. The stresses through thickness of SSSS Al/Al_2O_3 FG plate under sinusoidal load with $a/h=4$ (a) axial stress $\bar{\sigma}_{xx}$; (b) shear stress $\bar{\tau}_{yz}$.

Next, the bending behavior of SSSS porous FG (Al/Al_2O_3) plates with different porosity distributions and porosity volume fractions under sinusoidal load are considered. Table 3 depicts the normalized deflection at the central of the porous FG plates various porosity distribution, porosity volume fraction, material index and thickness ratio a/h. In addition, Fig. 16 examines the effects of porosity volume fraction and material index on the deflection of porous FG plates whose thickness ratio is $a/h=10$ with two porosity distributions, respectively. It is found that increasing the porosity volume fraction leads to larger deflections of FG plate since the higher density of internal pores decreases the plate stiffness. For both even and uneven distributions, by increasing the material index n, the bending stiffness of porous FG plate reduces which leads to higher deflection of porous FG plates. Moreover, the porous FG plate with even distribution have higher deflection than the other distribution with the same porosity volume fraction and thickness ratio a/h, especially with high values of α. This is to be expected since the even distribution provides the lowest effective stiffness of plate.

Table 3
The normalized central deflections $\bar{w}$ of porous FG $\left(Al/Al_2O_3\right)$ square plates under sinusoidal load.

		Even distribution				Uneven distribution			
a/h	α	$n=0$	$n=0.1$	$n=0.5$	$n=1$	$n=0$	$n=0.1$	$n=0.5$	$n=1$
4	0	0.3784	0.4161	0.5651	0.7279	0.3784	0.4161	0.5651	0.7279
	0.2	0.4292	0.4788	0.6969	0.9929	0.3950	0.4361	0.6040	0.8011
	0.4	0.4958	0.5637	0.9186	1.6831	0.4137	0.4587	0.6505	0.8968
10	0	0.2956	0.3274	0.4531	0.5882	0.2956	0.3274	0.4531	0.5882
	0.2	0.3353	0.3771	0.5634	0.8182	0.3054	0.3395	0.4793	0.6409
	0.4	0.3874	0.4448	0.7532	1.4502	0.3160	0.3527	0.5096	0.7086
100	0	0.2802	0.3109	0.4323	0.5622	0.2802	0.3109	0.4323	0.5622
	0.2	0.3179	0.3582	0.5385	0.7858	0.2888	0.3216	0.4562	0.6113
	0.4	0.3672	0.4226	0.7224	1.4069	0.2979	0.3330	0.4835	0.6739

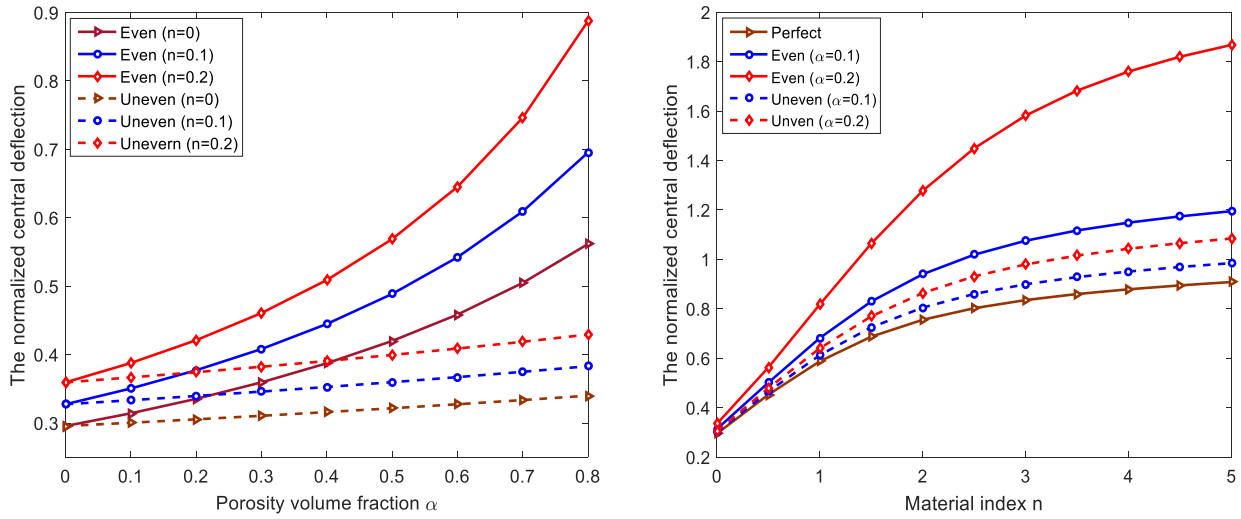

(a) (b)

Fig. 16. Effects of (a) porosity volume fraction and (b) material index on the normalized central deflections of porous FG plate $(a/h=10)$ under sinusoidal load.

4.2.2 Geometrically nonlinear analysis

Firstly, a fully clamped (CCCC) isotropic square plate which is subjected to uniform loading is considered in this section. The aspect ratio $a/h=100$ is considered. The material properties are given as follows: Young's modulus $E=3x10^7$ psi and Poisson's ratio $v=0.316$. For the efficient presentation of the results, the normalized central deflection $\bar{w}$, load parameter P and normal stress in the nonlinear analysis can be defined as

$$\bar{w}=\frac{w}{h},\quad P=\frac{q_0a^4}{E_mh^4},\quad \bar{\sigma}=\frac{\sigma a^2}{E_mh^2}. \tag{46}$$

Table 4 describes the normalized central deflection and normal stress of square isotropic plate for both linear and geometrically nonlinear cases. These results are then compared with those of other researchers including Levy's analytical solution [73], Nguyen *et al.* based on a refined quasi-3D IGA based on modified couple stress theory [74], Kant and Kommineni's C^0–FEM based on a higher-order theory [75], Urthaler and Reddy's mixed FEM based on FSDT [76]. As can be observed, the obtained results agree well with the analytical solutions and other reference results for both normalized deflection and normal stress. For further illustration, Fig. 17 performs the normalized deflections and normal stress at the central of plate for both linear and geometrically nonlinear cases. As expected, the deflection of geometrically nonlinear analysis becomes much smaller than that of linear analysis.

Table 4
Comparison of normalized central deflection $\bar{w}\left(a/2,a/2,0\right)$ and normal stress $\bar{\sigma}_x\left(a/2,a/2,h/2\right)$ of CCCC isotropic square plate under uniform load with $a/h=100$.

P	Response	Nonlinear					Linear	
		Present	Analytical [73]	IGA-RPT [74]	C^0-FEM [75]	MXFEM [76]	Present	MXFEM [76]
17.79	$\bar{w}$	0.237	0.237	0.2365	0.2385	0.2328	0.2441	0.2465
	$\bar{\sigma}_x$	2.5788	2.6	2.5602	2.6733	2.414	2.4849	2.387
38.3	$\bar{w}$	0.4704	0.471	0.4692	0.4725	0.4738	0.5255	0.5307
	$\bar{\sigma}_x$	5.3568	5.2	5.3256	5.5733	5.022	5.3498	5.138
63.4	$\bar{w}$	0.6927	0.695	0.6908	0.6948	0.6965	0.8699	0.8785
	$\bar{\sigma}_x$	8.1326	8.0	8.0973	8.4867	7.649	8.8558	8.510
95.0	$\bar{w}$	0.9049	0.912	0.9024	0.9065	0.9087	1.3034	1.3163
	$\bar{\sigma}_x$	10.855	11.1	10.8248	11.3500	10.254	13.27	12.745
134.9	$\bar{w}$	1.1093	1.121	1.1060	1.1100	1.1130	1.8509	1.8692
	$\bar{\sigma}_x$	13.54	13.3	13.5187	14.1700	12.850	18.843	18.099
184.0	$\bar{w}$	1.3049	1.323	1.3008	1.3046	1.3080	2.5245	2.5495
	$\bar{\sigma}_x$	16.185	15.9	16.1771	16.9367	15.420	25.701	24.686
245.0	$\bar{w}$	1.4978	1.521	1.4926	1.4963	1.5010	3.3614	3.3947
	$\bar{\sigma}_x$	18.897	19.2	18.9019	19.7633	18.060	34.222	32.869
318.0	$\bar{w}$	1.6846	1.714	1.6784	1.6820	1.6880	4.363	4.4062
	$\bar{\sigma}_x$	21.657	21.9	21.6744	22.6367	20.741	44.418	42.664
402.0	$\bar{w}$	1.8625	1.902	1.8552	1.8590	1.8660	5.5155	5.5702
	$\bar{\sigma}_x$	24.435	25.1	24.4624	25.5367	23.423	56.152	53.933

Next, the proposed method is further studied for simply supported Al/ZnO_2 square plates subjected to uniformly distributed load. The obtained results for various values of the material index n are compared to those of Nguyen et al. using isogeometric approach [74] and Praveen and Reddy [77] using FEM based on FSDT. It can be observed that a good agreement between the results obtained from the present approach and other reference solutions is obtained. The comparison of the nonlinear central deflection of simply supported square plates with different values of the material index n is depicted in Fig. 18.

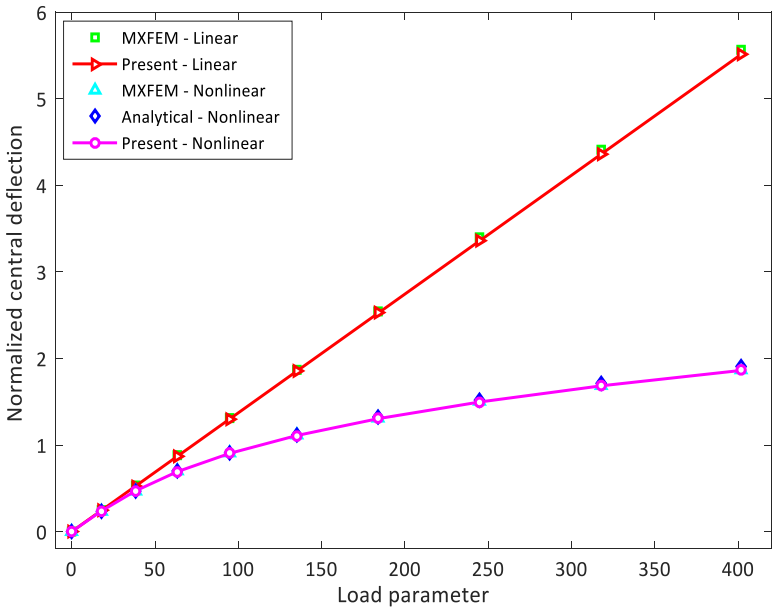

(a)

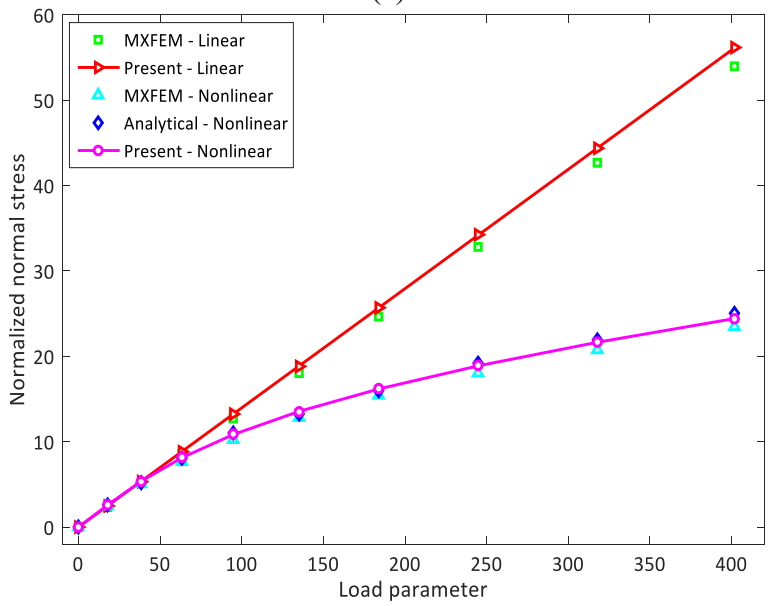

(b)

Fig. 17. Comparisons of nonlinear: (a) normalized central deflection and (b) normalized normal stress of fully clamped isotropic square plates with other published works.

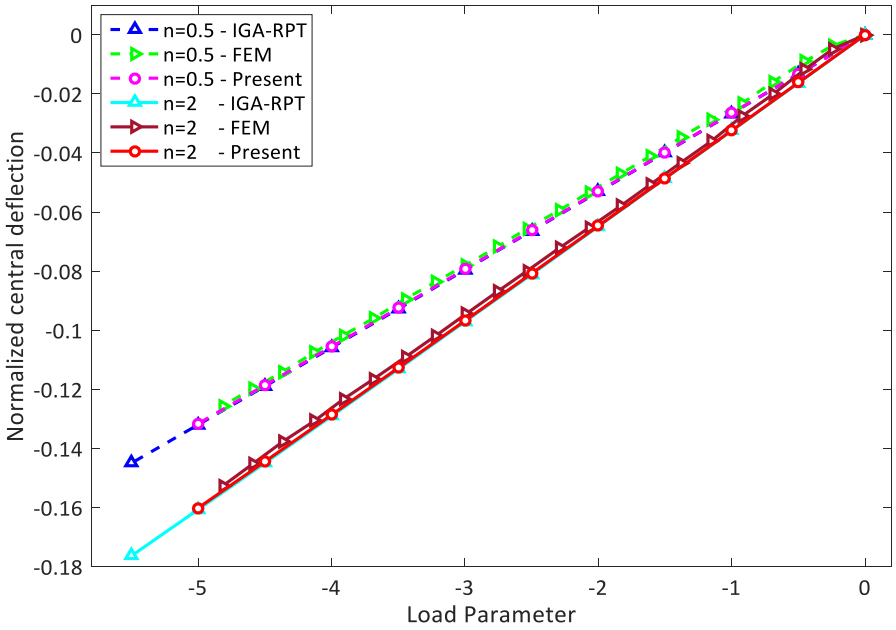

Fig. 18. Comparison of nonlinear normalized central deflection of a simply supported square Al/ZnO_2 under uniformly distributed load.

This section investigates the effects of the porosity volume fraction and the porosity distribution on the nonlinear normalized central deflection of porous FG (Al/ZnO_2) plates. Fig. 19 shows the nonlinear normalized central deflection of porous FG with the thickness ratio $a/h = 100$ and material index $n = 0.1$. It is clear that the porous FG plates have higher the deflection than a perfect FG plate. As evidently demonstrated in Fig. 19, at the same porosity volume fraction, the deflection of FG plates with even porosity distribution is much larger due to the reduction in the bending of the plate. Generally, the even porosity distribution significantly affects the defection of porous FG plate when the porosity volume fraction reach to high value, $\alpha = 0.6$ in this study. Conversely, the uneven porosity distribution is less sensitive to the porosity volume fraction since porosities vanish at the top and bottom surface of plate.

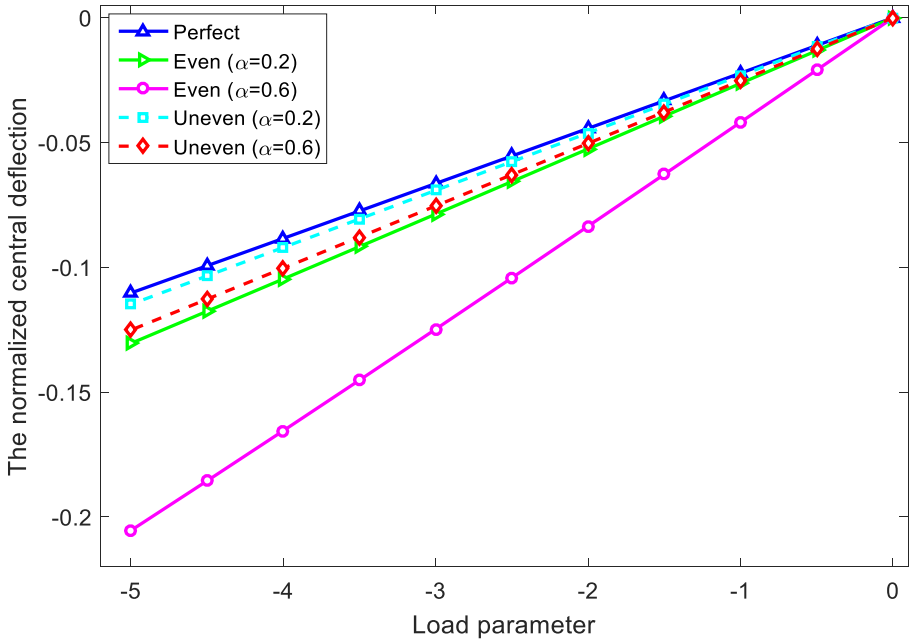

Fig. 19. The nonlinear normalized central deflection of porous FG plate.

4.3 Transient analysis of FG plate

In order to prove the reliability and the convergence of the present approach for transient problems, numerous numerical examples have been investigated to deal with the transient analysis of FG plates in this section. In all examples, the transverse load is sinusoidally distributed in short time $t_1 = 3$ milliseconds which is defined as follows: $q = q_0 \sin(\pi x / a)\sin(\pi y / a) F_0(t)$, where $q_0 = 15\text{MPa}$ and values of force $F_0(t)$ are presented in Fig. 20 depends on loading types such as step, triangular, sinusoidal and explosive blast, respectively.

$$F_0(t) = \begin{cases} \begin{cases} 1 & 0 \le t \le t_1, \\ 0 & t > t_1, \end{cases} & \text{Step load} \\ \begin{cases} 1 - t / t_1 & 0 \le t \le t_1, \\ 0 & t > t_1, \end{cases} & \text{Triangular load} \\ \begin{cases} \sin(\pi t / t_1) & 0 \le t \le t_1, \\ 0 & t > t_1, \end{cases} & \text{Sinusoidal load} \\ e^{-\gamma t}, & \text{Explosive blast load} \end{cases} \tag{47}$$

where $\gamma = 330\,\text{s}^{-1}$. The chosen time step Δt is $5x10^{-5}\,\text{s}$ in this study.

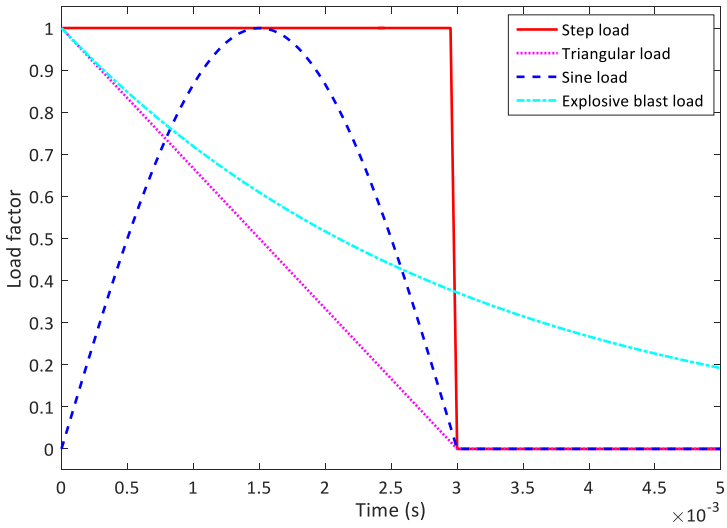

Fig. 20. Time history of load factor.

4.3.1 Linear dynamic analysis

The linear dynamic response analysis of the SSSS Al/Al_2O_3 square plate with $n=1$, which is subjected to a distributed sinusoidal load is considered in this section. The geometry of the square FG plate employed in this study is 0.2m in length and 0.01m in thickness. Its transient response according to the normalized central deflection $\bar{w}$ is depicted in Fig. 21. It is observed that the results obtained from the present approach agree well with those of IGA reported in [78].

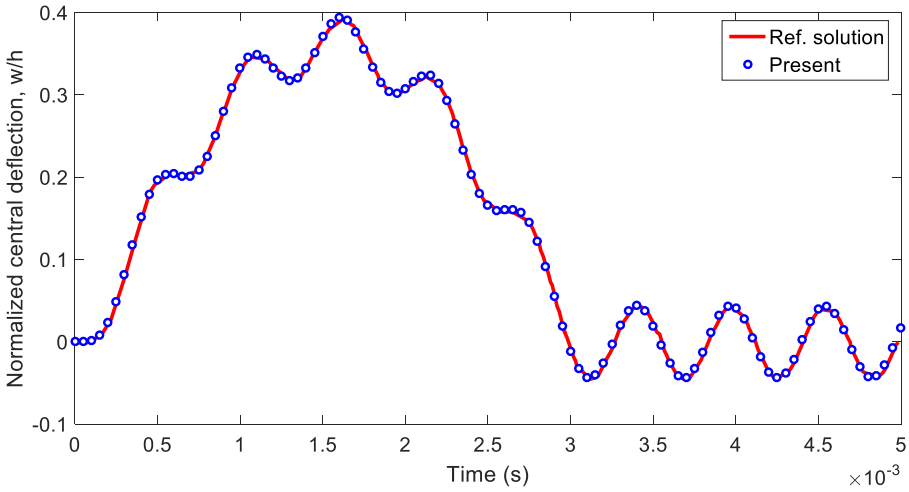

Fig. 21. Normalized linear transient central deflection of a simply supported square Al/Al_2O_3 plate under a sine load.

4.3.2 Geometrically nonlinear dynamic analysis

This section aims to verify the reliability of the proposed approach for the geometrically nonlinear transient analysis. An orthotropic SSSS square plate under a uniform step load with $q_0 = 1$ MPa is conducted. The material properties and the geometry of plate are considered as follows: Young's modulus $E_1 = 525$ GPa; $E_2 = 21$ GPa, shear modulus $G_{12} = G_{23} = G_{13} = 10.5$ GPa, Poisson's ratio $\nu = 0.25$, mass density $\rho = 800$ kg/m^3, length of the plate $L = 250$ mm and thickness $h = 5$ mm. Fig. 22 presents response of the plate to the loading. As expected, the obtained results are in an excellent agreement with the obtained from the finite strip method [79].

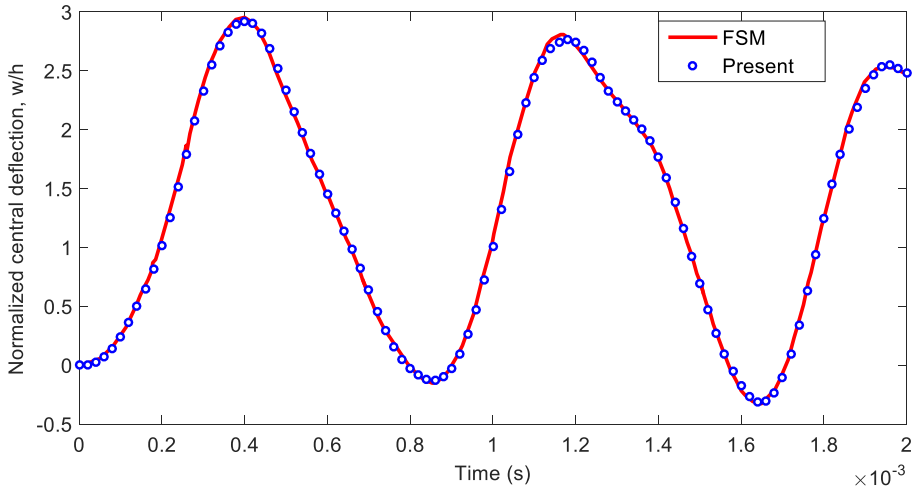

Fig. 22. Normalized nonlinear transient central deflection of a square orthotropic plate under uniform load.

Next, the normalized geometrically nonlinear transient response of deflection of the Al/Al_2O_3 plates without porosities which has length $L = 0.2$ and the thickness $h = 0.01$ are investigated. Fig. 23 illustrates time history of the normalized central displacement of perfect FG plate with $n = 1$ which is subjected to the step, triangular, sinusoidal and explosive blast load, respectively. As seen, the geometrically nonlinear transient responses to all types of loading give nearly same period of normalized central deflection, except for sinusoidal loading. Furthermore, the plates still deflect and vibrate harmonically after removing the applied load. The transient responses of linear and nonlinear of perfect FG plate with $n = 2$ under triangular are also depicted in Fig. 24.

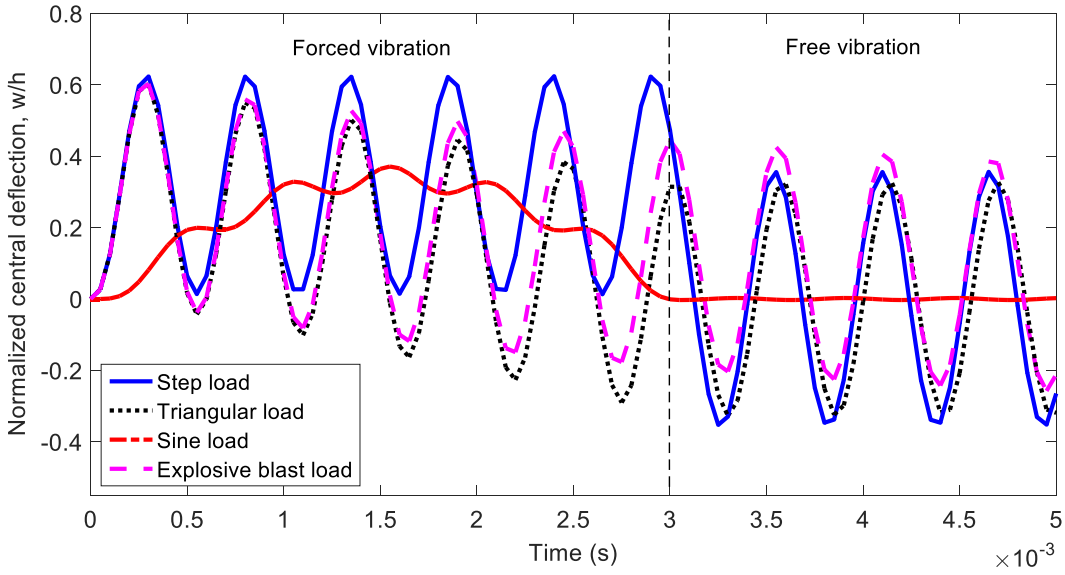

Fig. 23. Normalized nonlinear transient central deflection of perfect FG plate with $n=1$ under various loading types.

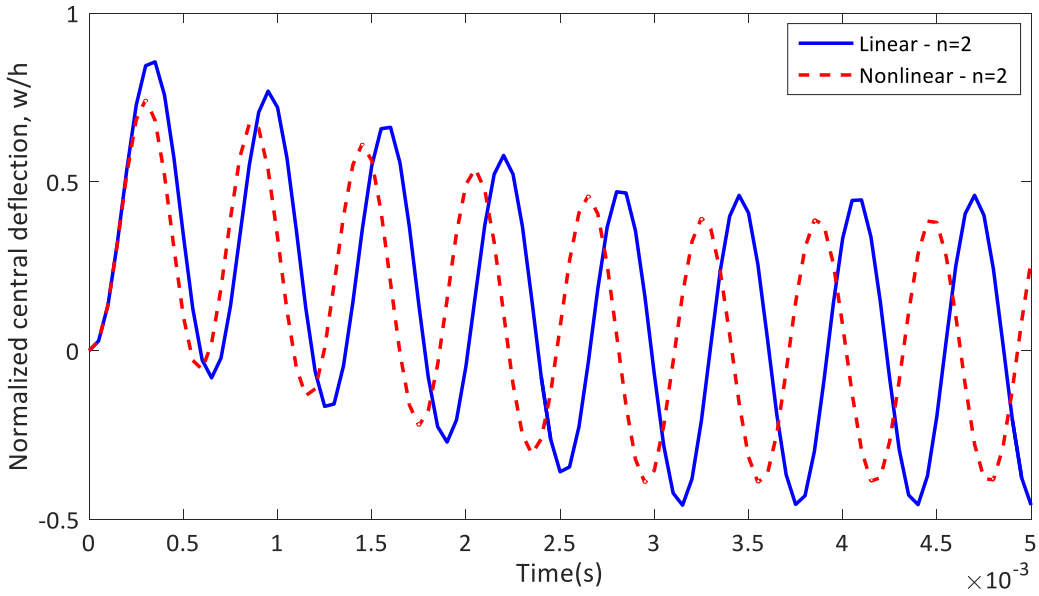

Fig. 24. Normalized linear and nonlinear transient deflection of perfect FG plate under triangular load with $n=2$.

The influences of the material index n on the geometrically nonlinear transient of normalized central deflection of a perfect FG plate with step load are described in Fig. 25. As can be seen, the increase of the material index n leads to the reduction of stiffness of plate due to more metal phrase in the plate volume. Consequently, the plates will vibrate with higher magnitude and period of the deflection.

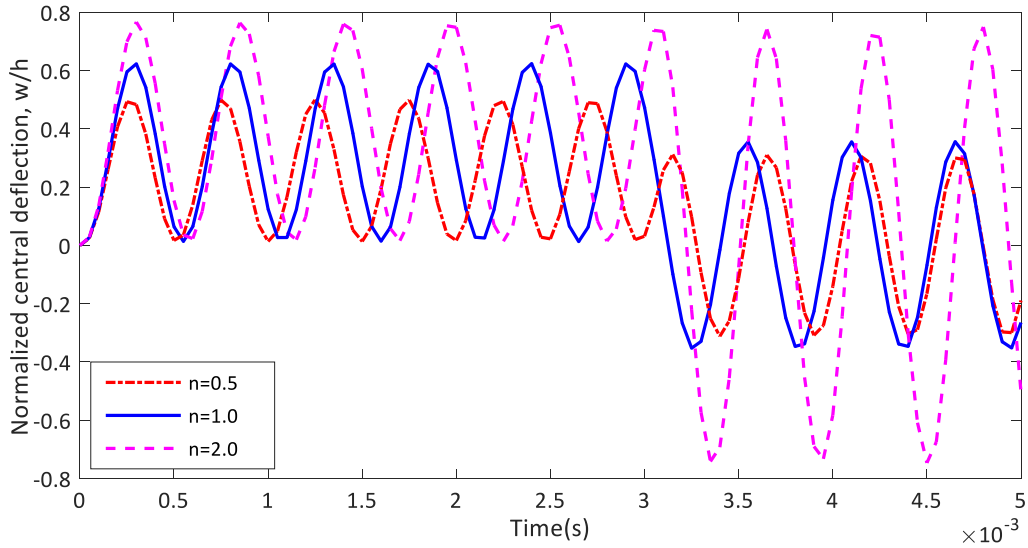

Fig. 25. Normalized nonlinear transient deflection of perfect FG plate under step load with various values of the material index.

In the last example, forced vibration responses of porous FG plate which is composed of Al and Al_2O_3 under explosive blast load with $n=1$ are investigated. The time histories of the normalized central displacement of porous FG plate with varying porosity volume fraction and distribution are displayed in Fig. 26. As previously discussed, an increase in the porosity volume fraction causes larger dynamic deflections. Moreover, this effect is more pronounced for porous FG plates with even porosity distribution.

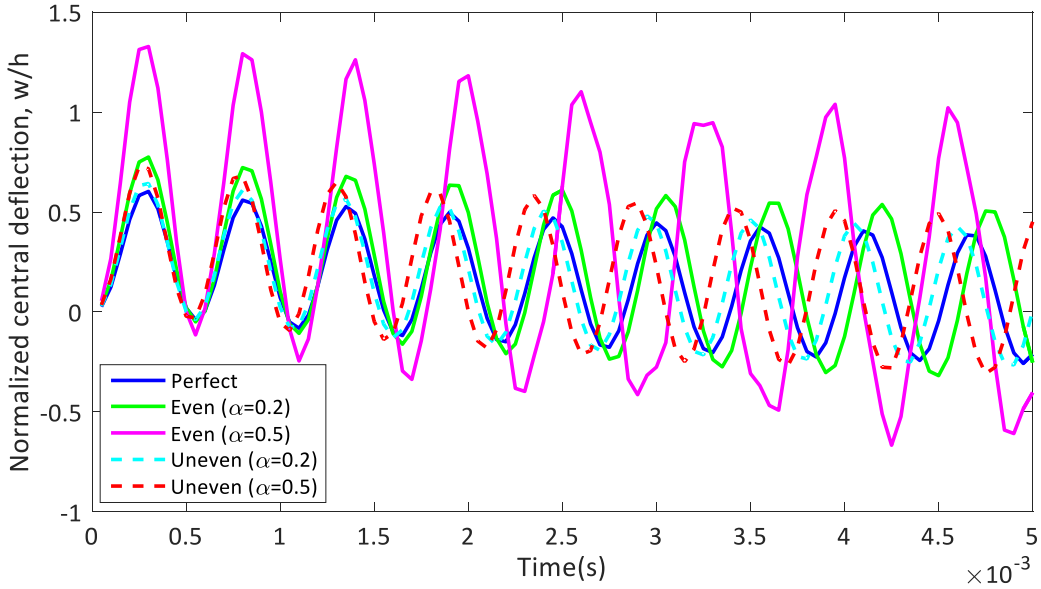

Fig. 26. Nonlinear transient deflection of porous FG plate under explosive blast load with $n=1$.

5. Conclusions

In this study, an efficient and novel unified PFEM formulation associated with quadratic serendipity shape functions and C^0-type HSDT model has been proposed to investigate static and dynamic problems of FG plates with porosities. The quadratic serendipity shape functions associated in vertices and mid-side nodes of the polygonal element were used to interpolate the bending strains while shear strains were calculated according to Wachspress coordinates at vertices of the polygonal elements. On the other hand, by using C^0-HSDT theory, the numerical results are more accurate and describe exactly the distribution of shear stress of FG plates without employing shear correction factors. Through the proposed formulations and numerical examples, several main conclusions are pointed out as follows:

- A novel unified PFEM associated with quadratic serendipity shape functions and C^0-type HSDT model for static and transient analyses which include both linear and geometrically nonlinear cases of FG plates with porosities was introduced.
- The effects of two porosity distributions and various porosity volume fractions on the deflection of porous FG plates are presented.
- Shear locking issue can be suppressed based on the Timoshenko's beam theory.
- With the same DOFs per polygonal element, the results which are generated from the proposed approach are stable and more accurate than other PFEMs which were based on the Wachspress and piecewise–linear basis functions.
- Finally, the proposed method could be extended to shell structures for future research work.

References

[1] M. Koizumi, The concept of FGM, Ceram. Trans. Funct. Grad. Mater. 34 (1993) 3–10.

[2] Y. Miyamoto, Functionally graded materials: design, processing, and applications, Dordrecht, Netherlands: Kluwer Academic Publications (1999).

[3] M. Naebe, K. Shirvanimoghaddam, Functionally graded materials: A review of fabrication and properties, Applied Materials Today 5 (2016) 223–245.

[4] C.H. Thai, A.J.M. Ferreira, M.A. Wahab, H. Nguyen-Xuan, A moving Kriging meshfree method with naturally stabilized nodal integration for analysis of functionally graded material sandwich plates, Acta Mechanica 229 (2018) 2997–3023.

[5] P. Phung-Van, C.-L. Thanh, H. Nguyen-Xuan, M.A. Wahab, Nonlinear transient isogeometric analysis of FG-CNTRC nanoplates in thermal environments, Compos. Struct. 201 (2018) 882-892.

[6] C.L. Thanh, P. Phung-Van, C.H. Thai, H. Nguyen-Xuan, M.A. Wahab, Isogeometric analysis of functionally graded carbon nanotube reinforced composite nanoplates using modified couple stress theory, Compos. Struct. 184 (2018) 633-649.

[7] P. Phung-Van, Loc V. Tran, A.J.M. Ferreira, H. Nguyen-Xuan, M.A. Wahab, Nonlinear transient isogeometric analysis of smart piezoelectric functionally graded material plates based on generalized shear deformation theory under thermo-electro-mechanical loads, Nonlinear Dyn. 87 (2017) 879-894.

[8] P. Phung-Van, A.J.M. Ferreira, H. Nguyen-Xuan, M.A. Wahab, An isogeometric approach for size-dependent geometrically nonlinear transient analysis of functionally graded nanoplates, Compos. B. Eng. 118 (2017) 125-134.

[9] P. Tan, N. Nguyen-Thanh, T. Rabczuk, K. Zhou, Static, dynamic and buckling analyses of 3D FGM plates and shells via an isogeometric-meshfree coupling approach, Compos. Struct.190 (2018) 35-50.

[10] P. Tan, N. Nguyen-Thanh, K. Zhou, Extended isogeometric analysis based on Bézier extraction for an FGM plate by using the two-variable refined plate theory, Theoretical and Applied Fracture Mechanics, 89 (2017) 127-138.

[11] N. Wattanasakulpong, B. Gangadhara Prusty, D.W. Kelly, M. Hoffman, Free vibration analysis of layered functionally graded beams with experimental validation, Mater. Des. 36 (2012) 182–190.

[12] N. Wattanasakulpong, V. Ungbhakorn, Linear and nonlinear vibration analysis of elastically restrained ends FGM beams with porosities, Aerosp. Sci. Technol. 32 (2014) 111–120.

[13] D. Chen, J. Yang, S. Kitipornchai, Free and forced vibrations of shear deformable functionally graded porous beams, Int. J. Mech. Sci. 108-109 (2016) 14–22.

[14] A.S. Rezaei, A.R. Saidi, Application of Carrera unified formulation to study the effect of porosity on natural frequencies of thick porous-cellular plates, Compos. B. Eng. 91 (2016) 361–370.

[15] Y.Q. Wang, Y.H. Wan, Y.F. Zhang, Vibrations of longitudinally traveling functionally graded material plates with porosities, Eur. J. Mech. A/Solids 66 (2017) 55-68.

[16] A.S. Rezaei, A.R. Saidi, M. Abrishamdari, M.H. Pour Mohammadi, Natural frequencies of functionally graded plates with porosities via a simple four variable plate theory: An analytical approach, Thin-Walled Struct. 120 (2017) 366–377.

[17] Y. Wang, D. Wu, Free vibration of functionally graded porous cylindrical shell using a sinusoidal shear deformation theory, Aerosp. Sci. Technol. 66 (2017) 83–91.

[18] M. Grygorowicz, K. Magnucki, M. Malinowski, Elastic buckling of a sandwich beam with variable mechanical properties of the core, Thin-Walled Struct. 87 (2015) 127–132.

[19] E. Magnucka-Blandzi, Axi-symmetrical deflection and buckling of circular porous-cellular plate, Thin-Walled Struct. 46 (2008) 333–337.

[20] A.M. Zenkour, A quasi-3D refined theory for functionally graded single-layered and sandwich plates with porosities, Compos. Struct. 201 (2018) 38–48.

[21] E. Reissner, The effect of transverse shear deformation on the bending of elastic plates, J. Appl. Mech. 12 (1945) 69–77.

[22] R. Mindlin, Influence of rotary inertia and shear on flexural motions of isotropic, elastic plates, J. Appl. Mech. 18 (1951) 31–38.

[23] J.N. Reddy, A simple higher-order theory for laminated composite plates, J. Appl. Mech. 51 (1984) 745–752.

[24] J.N. Reddy, Analysis of functionally graded plates, Int. J. Numer. Method Eng. 47 (2000) 663–684.

[25] A.M. Zenkour, Generalized shear deformation theory for bending analysis of functionally graded plates, Appl. Math. Modelling 30 (2006) 67–84.

[26] N. El Meiche, A. Tounsi, N. Ziane, I. Mechab, A new hyperbolic shear deformation theory for buckling and vibration of functionally graded sandwich plate, Int. J. Mech. Sci. 53 (2011) 237–247.

[27] S. Benyoucef, I. Mechab, A. Tounsi, A. Fekrar, H.A. Atmane, Bending of thick functionally graded plates resting on Winkler–Pasternak elastic foundations, Mech. Compos. Mater. 46 (2010) 425–434.

[28] N. Senthilnathan, S. Lim, K. Lee, S. Chow, Buckling of shear-deformable plates, AIAA journal 25 (1987) 1268–1271.

[29] A. Neves, A. Ferreira, E. Carrera, C. Roque, M. Cinefra, R. Jorge, C. Soares, A quasi-3D sinusoidal shear deformation theory for the static and free vibration analysis of functionally graded plates, Compos. B. Eng. 43 (2012) 711–725.

[30] E. Carrera, S. Brischetto, A. Robaldo, Variable kinematic model for the analysis of functionally graded material plates, AIAA J. 46 (2008) 194-203.

[31] C. Shankara, N. Iyengar, A C^0–element for the free vibration analysis of laminated composite plates, J. Sound Vib. 191 (1996) 721–738.

[32] H. Chi, C. Talischi, O. Lopez-Pamies, G. H. Paulino, Polygonal finite elements for finite elasticity, Int. J. Numer. Method Eng. 101 (2015) 305–328.

[33] K. Sze, N. Sheng, Polygonal finite element method for nonlinear constitutive modeling of polycrystalline ferroelectrics, Finite Elem. Analysis Des. 42 (2005) 107–129.

[34] A. Simone, C. Duarte, E. Van der Giessen, A generalized finite element method for polycrystals with discontinuous grain boundaries, Int. J. Numer. Method Eng. 67 (2006) 1122–1145.

[35] A. Menk, S. Bordas, Numerically determined enrichment functions for the extended finite element method and applications to bi-material anisotropic fracture and polycrystals, Int. J. Numer. Method Eng. 83 (2010) 805–828.

[36] H. Chi, C. Talischi, O. Lopez-Pamies, G.H. Paulino, A paradigm for higher-order polygonal elements in finite elasticity using a gradient correction scheme, Comput. Methods Appl. Mech. Eng. 306 (2016) 216–251.

[37] C. Talischi, A. Pereira, G.H. Paulino, I.F. Menezes, M.S. Carvalho, Polygonal finite elements for incompressible fluid flow, Int. J. Numer. Meth. Fluids 74 (2014) 134–151.

[38] A. Pereira, C. Talischi, G.H. Paulino, I.F. Menezes, M.S. Carvalho, Fluid flow topology optimization in PolyTop: stability and computational implementation, Struct. Multidiscip. Optim. 54 (2016) 1345–1364.

[39] A. Tabarraei, N. Sukumar, Extended finite element method on polygonal and quadtree meshes, Comput. Methods Appl. Mech. Eng. 197 (2008) 425–438.

[40] A. Khoei, R. Yasbolaghi, S. Biabanaki, A polygonal finite element method for modeling crack propagation with minimum remeshing, Int. J. Fract. 194 (2015) 123–148.

[41] H. Nguyen-Xuan, S. Nguyen-Hoang, T. Rabczuk, K. Hackl, A polytree-based adaptive approach to limit analysis of cracked structures, Comput. Methods Appl. Mech. Eng. 313 (2017) 1006–1039.

[42] K. N. Chau, K. N. Chau, T. Ngo, K. Hackl, H. Nguyen-Xuan, A polytree-based adaptive polygonal finite element method for multi-material topology optimization, Comput. Methods Appl. Mech. Eng. 332 (2018) 712-739.

[43] A.L. Gain, G.H. Paulino, L.S. Duarte, I.F. Menezes, Topology optimization using polytopes, Comput. Methods Appl. Mech. Eng. 293 (2015) 411–430.

[44] H. Nguyen-Xuan, A polytree-based adaptive polygonal finite element method for topology optimization, Int. J. Numer. Method Eng. 110 (2017) 972–1000.

[45] S. Biabanaki, A. Khoei, P. Wriggers, Polygonal finite element methods for contact-impact problems on non-conformal meshes, Comput. Methods Appl. Mech. Eng. 269 (2014) 198–221.

[46] H. Nguyen-Xuan, A polygonal finite element method for plate analysis, Comput. Struct. 188 (2017) 45–62.

[47] N.V. Nguyen, H.X. Nguyen, D.H. Phan, H. Nguyen-Xuan, A polygonal finite element method for laminated composite plates, Int. J. Mech. Sci. 133 (2017) 863–882.

[48] E.L. Wachspress, A rational finite element basis, Elsevier (1975).

[49] M.S. Floater, Mean value coordinates, Comput. aided geometric design 20 (2003) 19–27.

[50] K. Hormann, N. Sukumar, Maximum entropy coordinates for arbitrary polytopes, In Computer Graphics Forum 27 (2008) 1513-1520.

[51] N. Sukumar, B. Moran, A. Yu Semenov, V. Belikov, Natural neighbour Galerkin methods, Int. J. Numer. Method Eng. 50 (2001) 1–27.

[52] J. Manson, S. Schaefer, Moving least squares coordinates, In Computer Graphics Forum 29 (2010) 1517–1524.

[53] M.S. Floater, K. Hormann, G. Kós, A general construction of barycentric coordinates over convex polygons, Advances in Computational Mathematics, 24 (2006) 311-331.

[54] N. Sukumar, E. Malsch, Recent advances in the construction of polygonal finite element interpolants, Arch. Comput. Methods Eng. 13 (2006) 129–163.

[55] A. Rand, A. Gillette, C. Bajaj, Quadratic serendipity finite elements on polygons using generalized barycentric coordinates, Math. Comput. 83 (2014) 2691–2716.

[56] M. Sellam, S. Natarajan, K. Kannan, Smoothed polygonal finite element method for generalized elastic solids subjected to torsion, Comput. Struct. 188 (2017) 32–44.

[57] H. Chi, C. Talischi, O. Lopez-Pamies, G.H. Paulino, A paradigm for higher-order polygonal elements in finite elasticity using a gradient correction scheme, Comput. Methods Appl. Mech. Eng. 306 (2016) 216–251.

[58] M. Floater, M.-J. Lai, Polygonal spline spaces and the numerical solution of the poisson equation, SIAM J. on Numer. Analysis 54 (2016) 797–824.

[59] A. Sinu, S. Natarajan, K. Shankar, Quadratic serendipity finite elements over convex polyhedra, Int. J. Numer. Method Eng. 113 (2018) 109–129.

[60] N. Sukumar, Quadratic maximum-entropy serendipity shape functions for arbitrary planar polygons, Comput. Methods Appl. Mech. Eng. 263 (2013) 27–41.

[61] A. Soh, Z. Long, S. Cen, A new nine DOF triangular element for analysis of thick and thin plates, Comput. Mech. 24 (1999) 408–417.

[62] A.-K. Soh, S. Cen, Y.-Q. Long, Z.-F. Long, A new twelve DOF quadrilateral element for analysis of thick and thin plates, Eur. J. Mech. A/Solids 20 (2001) 299–326.

[63] T. Nakamura, T. Wang, S. Sampath, Determination of properties of graded materials by inverse analysis and instrumented indentation, Acta Mater. 48 (2000) 4293–4306.

[64] J.N. Reddy, An Introduction to Nonlinear Finite Element Analysis, Oxford University Press, Oxford (2004).

[65] N.M. Newmark, A method of computation for structural dynamics, J. Eng. Mech. Div. ASCE 85 (1959) 67–94.

[66] S. Thai, H.T. Thai, T.P. Vo, J.N. Reddy, Post-buckling of functionally graded microplates under mechanical and thermal loads using isogeomertic analysis, Eng. Struct. 150 (2017) 905–917.

[67] J.N. Reddy, Geometrically nonlinear transient analysis of laminated composite plates, AIAA J. 21 (1983) 621–629.

[68] R.L. Taylor, F. Auricchio, Linked interpolation for Reissner-Mindlin plate elements: part II - a simple triangle, Int. J. Numer. Method Eng. 36 (1993) 3057–3066.

[69] H. Nguyen-Xuan, T. Rabczuk, S. Bordas, J.F. Debongnie, A smoothed finite element method for plate analysis, Comput. Methods Appl. Mech. Eng. 197 (2008) 1184–1203.

[70] E. Carrera, S. Brischetto, M. Cinefra, M. Soave, Effects of thickness stretching in functionally graded plates and shells, Compos. B. Eng. 42 (2011) 123–133.

[71] T.-K. Nguyen, V.-H. Nguyen, T. Chau-Dinh, T.P. Vo, H. Nguyen-Xuan, Static and vibration analysis of isotropic and functionally graded sandwich plates using an edge-based MITC3 finite elements, Compos. B. Eng. 107 (2016) 162–173.

[72] A. Neves, A. Ferreira, E. Carrera, M. Cinefra, C. Roque, R. Jorge, C.M. Soares, Static, free vibration and buckling analysis of isotropic and sandwich functionally graded plates using a quasi-3D higher-order shear deformation theory and a meshless technique, Compos. B. Eng. 44 (2013) 657–674.

[73] S. Levy, Square plate with clamped edges under normal pressure producing large deflections, Tech. Rep. 740, National Advisory Committee for Aeronautics (1942).

[74] H.X. Nguyen, E. Atroshchenko, H. Nguyen-Xuan, T.P. Vo, Geometrically nonlinear isogeometric analysis of functionally graded microplates with the modified couple stress theory, Comput. Struct. 193 (2017) 110–127.

[75] T. Kant, J.R. Kommineni, C^0 Finite element geometrically non-linear analysis of fibre reinforced composite and sandwich laminates based on a higher-order theory, Comput. Struct. 45 (1992) 511–520.

[76] Y. Urthaler, J.N. Reddy, A mixed finite element for the nonlinear bending analysis of laminated composite plates based on FSDT, Mech. Adv. Mater. Structures, 15 (2008) 335–354.

[77] G.N. Praveen, J.N. Reddy, Nonlinear transient thermoelastic analysis of functionally graded ceramic-metal plates, Int. J. Solids Struct. 35 (1998) 4457–4476.

[78] L. Tran Vinh, Isogeometric analysis for functionally graded plates using higher order shear deformation theory, Ghent University, Faculty of Engineering and Architecture (2016).

[79] J. Chen, D.J. Dawe, S. Wang, Nonlinear transient analysis of rectangular composite laminated plates, Compos. Struct. 49 (2000) 129–139.